Keio University

CALAMVS GLADIO FORTIOR

1858

# Annual Report on Research Activities 2016

Tanabe Photonic Structure Group,

Department of Electronics and Electrical Engineering,

Faculty of Science and Technology, Keio University

# Contents

# Foreword

I would like to express my great thanks to whom supporting the research and education in our group; Tanabe Photonic Nanostructure Laboratory, in the Department of Electronic Engineering, Keio University.

Two PhD students graduated this year, who are among the first students, joined our lab when our laboratory started six year ago. These two students completed their leading-graduate school program (all-round type), where they pursued a double-degree program (MMD). They are the first student who received two master degrees, one from science and one from humanities, and a PhD from science and technology. I am proud to both students who will bring broad new aspect to the field. Another two students who are currently enrolled in the PhD course is now receiving the research fellowship for young scientist (DC1, DC2) from the Japan Society for the Promotion of Science (JSPS), which allow them to focus on research activities.

It is now becoming increasingly important to be a part of global research community to pursue good and global researches. This year, we invited researchers from IMRA America and Harvard University to deliver seminars in Yagami Campus. The interaction is very important for my students to get stimulated. We will continue build connection with groups from different background and regions. If you are interested in our research, please do not hesitate to contact us.

Here, we will report our research activities in FY2016. You may realize that some of the manuscript are difficult to read, since these manuscripts are written by my students with minimum language editing. However, I am confident that all the research conducted by my members is of high level and will contribute significantly to the community. If you are interested in our research, please contact us.

October 2017
Takasumi Tanabe, Associate Professor,
Department of Electronics and Electrical Engineering,
Keio University

# Lab Members (Names and their positions after graduation)

**Associate Professor:** Takasumi Tanabe

**Secretary:** Naoko Kojima

**PhD Students:**

| | |
|---|---|
| Nurul Ashikin Binti Daud | |
| | Continues in the graduate school of Keio University |
| Wataru Yoshiki | Continues in the graduate school of Keio University |
| | Leading Graduate School RA (all-round type) |
| Takumi Kato | Continues in the graduate school of Keio University |
| | Leading Graduate School RA (all-round type) |
| Ryo Suzuki | Continues in the graduate school of Keio University |
| | Leading Graduate School RA (global environment system leader) |
| | Research Fellowship for Young Scientist, JSPS (DC1) |
| Tomohiro Tetsumoto | Continues in the graduate school of Keio University |
| | Research Fellowship for Young Scientist, JSPS (DC2) |

**Master 2nd Grade: (The class of 2014)**

| | |
|---|---|
| Hiroki Itobe | Graduates the graduate school of Keio University |
| Yuta Ooka | Graduates the graduate school of Keio University |
| Yusuke Okabe | Graduates the graduate school of Keio University |
| Misako Kobayashi | Graduates the graduate school of Keio University |
| Takuma Nagano | Graduates the graduate school of Keio University |

**Master 1st Grade: (The class of 2015)**

| | |
|---|---|
| Hajime Kumazaki | Continues in the graduate school of Keio University |
| Naoya Hirota | Continues in the graduate school of Keio University |
| Shun Fujii | Continues in the graduate school of Keio University |
| Atsuhiro Hori | Continues in the graduate school of Keio University |

**Bachelor 4th Grade: (The class of 2016)**

| | |
|---|---|
| Takumi Okamura | Enters graduate school of Keio University |
| Naotaka Kamioka | Enters graduate school of Keio University |
| Akihiro Kubota | Enters graduate school of Keio University |
| Mika Fuchida | Enters graduate school of Keio University |
| Yoshihiro Honda | Enters graduate school of Keio University |

# Research Activities

# Adiabatic frequency conversion using the Kerr effect in an ultra-high-$Q$ silica toroid microcavity

Wataru Yoshiki (D3), Yoshihiro Honda (B4), Misako Kobayashi (M2), Tomohiro Tetsumoto (D2)

We report the first demonstration of adiabatic frequency conversion using the Kerr effect in a silica toroid microcavity. Taking advantage of the instantaneous response of the Kerr effect, we achieved adiabatic frequency conversion with a controllable amount of frequency shift and time width. In addition, thanks to the combination of the Kerr effect and the ultra-high $Q$ (>$10^7$) of the silica toroid microcavity, we also observed multiple frequency conversion within a photon lifetime.
**Key words:** Silica toroid microcavity; Adiabatic frequency conversion; Ker effect;

## 1. Introduction

When the resonant frequency of an optical microcavity in which light is trapped is shifted very quickly, the frequency of the light is also changed following the shift. This phenomenon is known as adiabatic frequency conversion (AFC), and has already been observed with a microring [1] and a photonic crystal nanocavity [2]. In these previous studies the resonant frequency was controlled by exciting free carriers in the cavity via the irradiation of high-power "control" pulses. This results in the AFC of a "signal" light (see Fig. 1). However, the carrier's finite diffusion time limits AFC controllability. For example, as shown in Fig. 1, the shifted resonance does not return to the original frequency even after the control pulse has been turned off. In addition, free-carrier absorption induces an additional loss, which makes the carrier-induced AFC unsuitable for loss-sensitive applications such as quantum optics.

In this paper, we report the first demonstration of AFC in a silica toroid microcavity using the Kerr effect [3]. A silica toroid microcavity [4] is employed as a platform for the experiments because its ultra-high $Q$ factor provides a long operation time for AFC, and its large bandgap prevents the generation of free carriers. The Kerr effect responds instantaneously (Fig. 1), thus it allows us to achieve AFC with high controllability of such characteristics as the amount of conversion, the conversion time width, and the number of conversions. Even multiple AFC within a photon lifetime is possible.

## 2. Experimental setup and procedure

Although the Kerr effect is advantageous as regards a fast response and a low loss, it does not induce a refractive index change as large as that induced by the carrier-plasma effect. This infers that we need to couple a control pulse with the resonant mode in the cavity to obtain a sufficiently large refractive index change. However, if the resonance is utilized, the AFC response time is limited by the photon lifetime. This becomes an issue because AFC occurs only when the resonance is shifted in less than the photon lifetime. Taking this into consideration, we employed ultra-high ($1.9 \times 10^7$) and moderate $Q$ ($1.8 \times 10^6$) modes, respectively, for the signal and control lights. In this condition, the photon lifetime of the control mode becomes much shorter than that of the signal mode, thus making it possible to shift the frequency of the signal mode well within the photon lifetime of the signal mode.

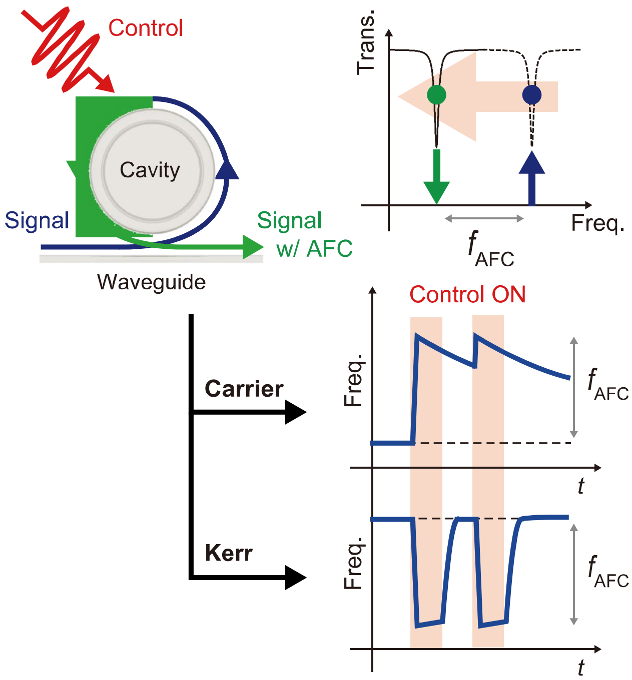


Fig 1 Schematic illustration of AFC.

Figure 2(a) depicts a block diagram of the experimental setup. The signal and control lights emitted from the tunable laser sources (TLSs) were both modulated into a rectangular pulse with intensity modulators (IMs). The control pulse was amplified with the erbium-doped fiber amplifier (EDFA) after the IM. The two lights were combined, and then input into a tapered optical fiber, and coupled into a microcavity. The output single light was measured with a photodetector (PD) and an oscilloscope after the control light was filtered out with a band-pass filter (BPF). Figure 2 shows the experimental procedure. Once the signal light is turned off, the signal output decays exponentially after exhibiting a rapid increase if there is no control input. However, if we input a control light (the red region in the figure), the resonance of the signal mode is shifted, and then the frequency of the light in the cavity also changes via AFC. In this situation, the frequency of light coupled out from the cavity differs from that of light transmitted through the fiber, which creates a beat in the signal output. The beat frequency is equal to the frequency shift induced by AFC ($f_{AFC}$). Therefore, observation of the beat proves the realization of AFC and gives us information on $f_{AFC}$.

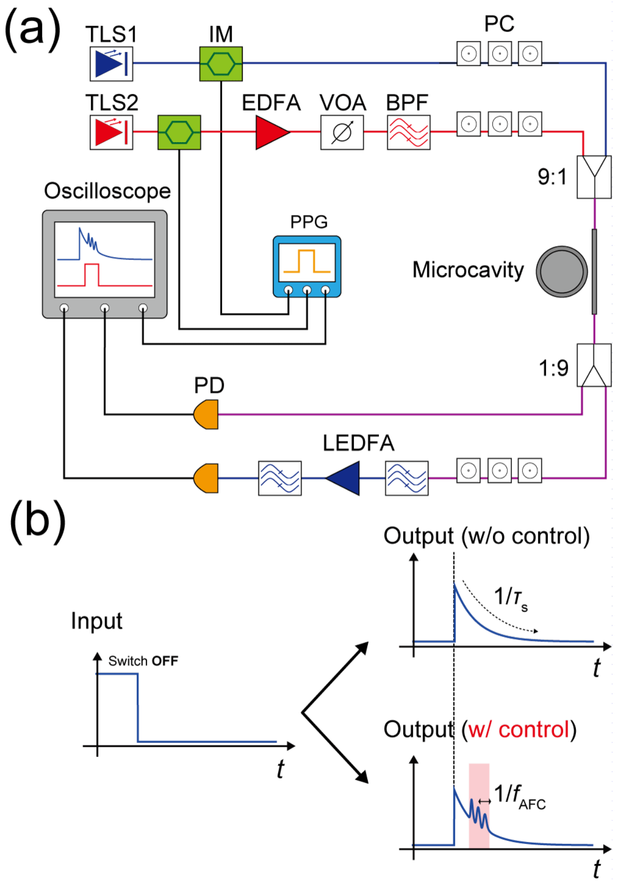


Fig 2 (a) Experimental setup for the AFC experiments. (b) Schematic illustration of how to observe AFC in the output signal light.

## 3. Experimental results

Figures 3(a)-(d) show experimental results. The output signal lights for different input control powers $P_c$ is shown in Fig. 3(a). As seen from the figure, the output signals have a beat while the control light is being input. The beat disappears immediately once the control light is turned off because the Kerr effect responds instantaneously. Such behavior is rarely observed with carrier-induced AFC [1,2] owing to its relatively slow diffusion time. The figure also indicates that the beat frequency (i.e. $f_{AFC}$) becomes higher as $P_c$ increases, and reaches 140 MHz, which is approximately 14 times the linewidth of the signal mode. Such behavior can also be seen in Fig. 3(c) where the relation between the input control power and $f_{AFC}$ is plotted. This behavior is intuitively understandable because the Kerr effect must be greater for a higher $P_c$. Figure 3(b) shows the signal output for different control pulse widths. It is clear from the figure that the time width of AFC can also be controlled by changing the time width of the control light thanks to the instantaneous response of the Kerr effect. Therefore, we can say that the time width of the Kerr-induced AFC is also controllable. Note that the red dashed lines in Figs. 3(a)-(c) were calculated by using coupled mode theory, which considers the Kerr effect, and they agree well with the experimental lines.

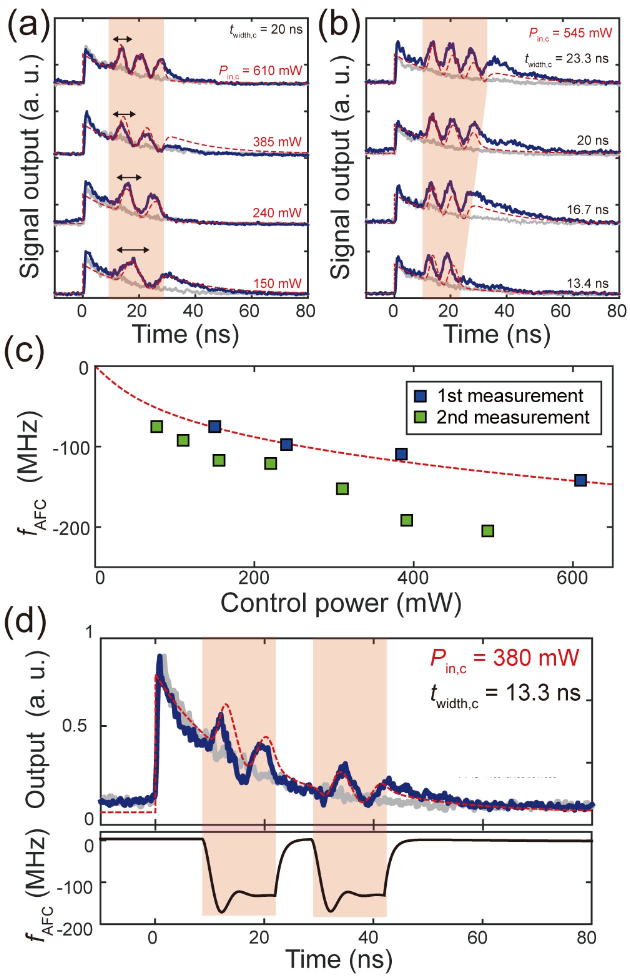


Fig 3 The output signal light for (a) a different input control power, (b) a different control pulse width, and (d) two input control pulses. The blue and gray curves represent the signal output with and without the control light, respectively. The control light is being input in the red regions. (c) The frequency shift for different input control powers. The red dashed curves in (a)–(d) are the calculated curves, and the black solid curve in the lower panel of (d) shows the calculated time-dependent frequency shift.

Finally, Fig. 3(d) shows the signal output when two control pulses are input while the signal output is decaying. There are two beats in the figure, and the experimental and calculated curves agree well. In addition, the time-dependent frequency shift obtained with the calculated curve implies that AFC occurs twice as presented in the lower panel of Fig. 3(d). Thus we can conclude that multiple AFC was performed within a photon lifetime.

In summary, Kerr-induced AFC was proven to have controllability as regards the amount of conversion (Fig. 3(a)), the conversion time width (Fig. 3(b)), and the number of conversions (Fig. 3(d)).

## 4. Conclusion

We described the first demonstration of AFC using the Kerr effect. We performed AFC with high controllability by combining the Kerr effect and the ultra-high *Q* factor of a silica toroid microcavity.

## References

[1] S. F. Preble, Q. Xu, and M. Lipson, Nat. Photonics **1**, 293 (2007).
[2] T. Tanabe, M. Notomi, H. Taniyama, and E. Kuramochi, Phys. Rev. Lett. **102**, 043907 (2009).
[3] W. Yoshiki, Y. Honda, M. Kobayashi, T. Tetsumoto, and T. Tanabe, Opt. Lett. **41**, 5482 (2016).
[4] D. Armani, T. Kippenberg, S. Spillane, and K. J. Vahala, Nature **421**, 925 (2003).

# Experimental demonstration of all-optical tunable buffering with ultra-high-*Q* whispering gallery mode microcavity

Wataru Yoshiki (D3), Yoshihiro Honda (B4), Tomohiro Tetsumoto (D2)

We present the first experimental demonstration of all-optical tunable buffering with coupled ultra-high *Q* whispering gallery mode (WGM) microcavities. Among various WGM cavities, we chose a silica toroid microcavity, which has an ultra-high *Q* factor, a small mode volume, and can be fabricated on a chip. The ultra-high *Q* (> 2 x $10^7$) allowed us to buffer an optical pulse for 20 ns.

**Key words:** Silica toroid microcavity; Coupled cavities; Optical buffer; Ker effect;

## 1. Introduction

All-optical buffering is crucial for various applications including all-optical signal processing. One promising platform for all-optical buffering is the electromagnetically-induced transparency (EIT) process by which a narrow transmission window is formed in an absorption spectrum under the irradiation of a control laser [1]. Recently, it was proven that coupled optical modes in optical cavities are capable of exhibiting an EIT-like phenomenon, which is called coupled mode-induced transparency (CMIT) [2]. In contrast to EIT, CMIT can be realized at room temperature, and does not require any atom-trapping techniques. Moreover, if CMIT is developed with microcavities, we can develop a compact all-optical buffer on a chip [3]. These features pave the way to the practical use of CMIT for all-optical buffering. More recently, Yanik *et al.* [4] revealed theoretically that the dynamic tuning of the cavity resonance provides CMIT-based all-optical buffering with "tunability". All-optical tunable buffering was later realized experimentally with coupled silicon microring cavities [5]. However, its maximum buffering time is no more than a few-hundred ps because the *Q* factor of the cavity stays very low (~$10^5$). Clearly, the maximum buffering time can be greatly improved by employing an ultra-high *Q* WGM microcavity, and CMIT has already been reported in various WGM cavities [6]. However, using it for all-optical tunable buffering is still difficult because the resonance of WGM cavities is not easy to tune "dynamically". Although thermo-optic and pressure-induced tunings are available in WGM microcavities [7,8], their speed is not very fast (>µs).

In this manuscript [9], we report an experimental demonstration of all-optical tunable buffering with coupled ultra-high *Q* microcavities. We used the Kerr effect to tune the cavity because it can change the refractive index almost instantaneously. This made it possible to tune the resonance of the WGM cavity quickly. We chose a silica toroid microcavity as the platform for our experiments because it has an ultra-high Q factor (> 2 x $10^7$) and a small mode volume, and can be fabricated on a chip [10]. Taking advantage of the silica toroid microcavity and the Kerr effect, we achieved all-optical tunable buffering with a maximum buffering time of 20 ns.

## 2. Working principle

We begin by describing the working principle of all-optical tunable buffering with coupled silica toroid microcavities. Here we assume a situation in which two silica toroid microcavities are coupled to each other (Fig. 1(a)). If the resonant frequencies of the two cavities ($C_1$ and $C_2$) match, the light input into a tapered optical fiber (i.e. "signal" light) first couples to $C_2$, and then moves to $C_1$ (see "(1) input" of the figure). While the light stays in $C_1$, an additional high-power light (i.e. "control" light) is input into another mode in $C_2$ as illustrated in "(2) buffer" of the figure. The input control light induces the Kerr effect, and then tunes the resonances of $C_2$, which creates a mismatch between the resonances of $C_1$ and $C_2$. This mismatch prevents the signal light from escaping from $C_2$, thus light is captured in $C_1$ while the control light is being input. After the control light is turned off, the resonances of the two cavities become matched again. In this condition, the signal light is now allowed to couple into $C_2$, then, it is output to the tapered optical fiber ("(3) output"). Therefore, the signal light can be buffered for an arbitrary time period by changing the duration of the control pulse in this system. This is the working principle of all-optical tunable buffering with coupled silica toroid microcavities.

## 3. Device fabrication and characterization

The silica toroid microcavities employed in the experiments ($C_1$ and $C_2$) were fabricated using five processes: (1) photolithography, (2) HF etching, (3) dicing, (4) $XeF_2$ dry etching, and (5) laser reflow. First, in (1) the photolithography process, circular resist patterns100 µm in diameter, were developed on a silicon chip with a 2 µm-thick silica layer.

Then, (2) HF etching removed only the parts of the silica layer that were not covered by the resist patterns. As a result, circular silica pads were formed on the silicon chip. Next, by using a high-precision dicing machine we cut part of the chip to allow us to place the silica pads near the edge of the chip ((3) dicing process). After that, (4) $XeF_2$ dry etching was used to undercut the silica pads, and then silica disks on a silicon pillar were fabricated. Because the pads were placed near the edge, parts of the disks protrude from the chip. This enabled us to position two microcavities very close together (see Fig. 1(b)). Finally, the fabrication was completed by irradiating the silica disks with a $CO_2$ laser and annealing them so that their surfaces became very smooth ((5) laser reflow process). Note that $C_1$ and $C_2$ were fabricated on different chips to control the gap between them during characterization.

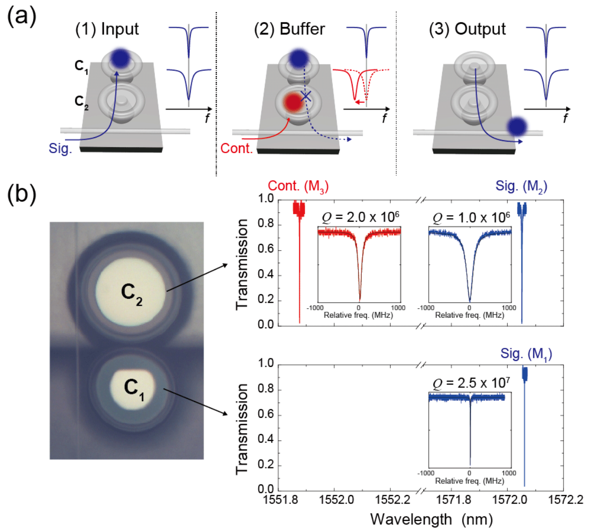


Fig 1 (a) Schematic illustration of all-optical tunable buffering. (b) Transmission spectra of $C_1$ and $C_2$.

The transmission spectra of the modes that were used for the experiments are shown in the graphs in Fig. 1(b). We selected two modes ($M_1$ and $M_2$) for the signal light and a mode ($M_3$) for the control mode from optical modes in $C_1$ and $C_2$. $M_1$ and $M_2$ couple to each other, thus the signal light input into $M_2$ is transferred into $M_1$ as illustrated in Fig. 1(a). On the other hand, $M_3$ does not couple to any modes because it is used only for inducing the Kerr effect in $C_2$. Note that the $Q$ factor of $M_1$ should be higher to obtain a longer maximum buffering time because the signal light is stored in $M_1$ during the buffering operation. Taking this into consideration, we selected a mode with a $Q$ of over $2 \times 10^7$ for $M_1$. On the other hand, the $Q$ factors of $M_2$ and $M_3$ should have moderate values. This is because a lower $Q$ results in not only a larger bandwidth but also a higher required control power. In addition, if $M_3$ is chosen from the same mode family as $M_2$, it should have the almost same $Q$ factor as $M_2$. Thus, we employed modes with $Q$ values of around $10^6$ for $M_2$ and $M_3$.

## 4. Experimental setup and results

Figure 2(a) shows the setup for all-optical tunable buffering. We employed two tunable laser sources (TLSs) to emit the signal and control lights. Both lights were modulated into rectangular pulses with intensity modulators (IMs). After modulation, the control light was amplified with an erbium-doped fiber amplifier (EDFA). Both lights were input into the coupled silica toroid microcavities via a tapered optical fiber, and at the output only the signal light was detected with an optical sampling oscilloscope (OSO) after amplification with an L-band EDFA (LEDFA). Note that the output control light was filtered out with a band pass filter (BPF) before the amplification. Coupling between $C_1$ and $C_2$ was achieved by placing them separately on automatic *xyz* stages and precisely controlling the gap between the two cavities. The resonant frequencies of $M_1$ and $M_2$ were matched by controlling the temperature of $C_1$ with a thermoelectric cooler (TEC) whose temperature was stabilized by using a TEC driver with a temperature stability of 2 mK.

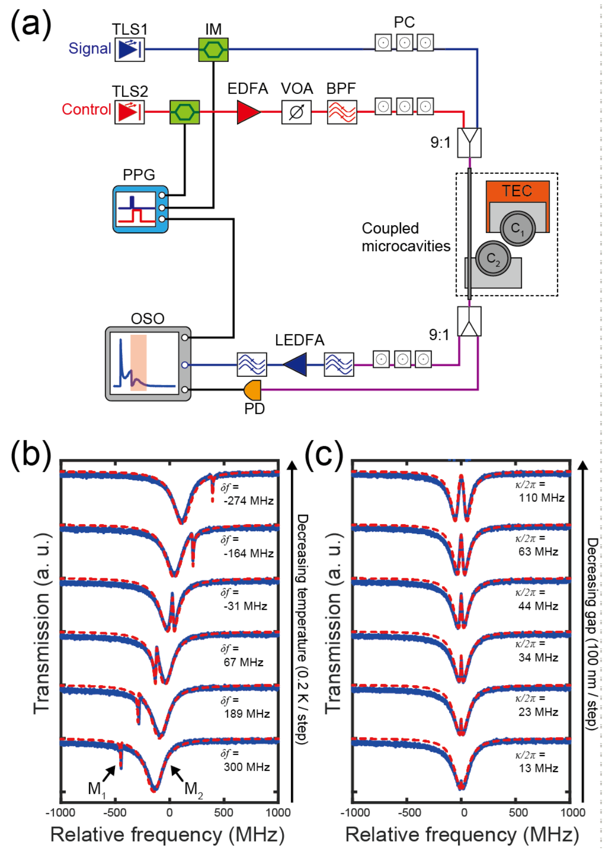


Fig 2 (a) Setup for all-optical tunable buffering. VOA: Variable optical attenuator. PC: Polarization controller. LEDFA: L-band EDFA. PD: Photodetector. PPG: Pulse pattern generator. (b,c) Transmission spectra of coupled $M_1$ and $M_2$ for different (b) temperatures of $C_1$ and (c) different gaps between $C_1$ and $C_2$, respectively.

Figure 2(b) shows the transmission spectra of the coupled $M_1$ and $M_2$ for different temperatures of $C_1$. As seen from each graph in the figure, there is a split in the transmission spectrum, which is direct evidence of coupling between the two modes. In addition, it shows a clear Fano resonance, which usually occurs when optical modes with very different $Q$ factors are coupled. The transmission spectra for the different gaps between the two cavities are displayed in Fig. 2(c). The split width (the coupling rate between $M_1$ and $M_2$) becomes larger as the gap decreases, which means that the coupling rate is arbitrarily adjustable with the gap. In the buffering experiments, the resonance frequencies of $M_1$ and $M_2$ were completely matched and the split width was adjusted to around 70 MHz. This is because too large a split width (i.e. higher coupling rate) results in a higher required control power.

Here we report our experimental results for all-optical tunable buffering. We measured the signal output for the control light with different pulse widths as shown in Figs. 4(a) and (b). As seen from the figures, all-optical tunable buffering appears to work well. The signal light pulse is stored while the control light is being input (indicated by the red region), and then it is coupled out after the control light is turned off. In addition, the figures also indicate that the buffering times can be controlled by changing the control pulse widths. In fact, we can experimentally buffer a signal pulse with a time width of 10 ns for up to 20 ns. This constitutes direct evidence proving that all-optical tunable buffering was achieved. Close observation of Fig. 4(b) infers that a small amount of the signal light leaks out while the control light is turned on. This is owing to the small coupling remaining between $M_1$ and $M_2$, which allows the signal light to escape to the tapered optical fiber through M2. However, the signal light leakage is believed to be small enough to have no influence on the buffering performance. This is because there was no change in the leakage when the input control power (i.e. the amount of resonance shift) was changed. In other words, the dominant loss source during buffering must be the intrinsic loss of $M_1$.

Finally we compare the obtained results with those of previous studies. A CMIT-based all-optical tunable buffer is advantageous thanks to its small size and capacity for on-chip fabrication. However, the previously-reported example [5] is composed of low-$Q$ cavities, and thus its maximum buffering time is limited to a few hundred ps. Although there are other types of on-chip all-optical tunable buffering that are achieved by the dynamic tuning of a waveguide-coupled photonic crystal nanocavity [11] and a photonic crystal slow light waveguide [12], they also have an issue as regards the buffering time. Conversely, in this study, all-optical tunable buffering exhibited a maximum buffering time of 20 ns thanks to the ultra-high $Q$ factor of the silica toroid microcavity. Therefore, we can conclude that our buffer is advantageous in terms of the maximum buffering time.

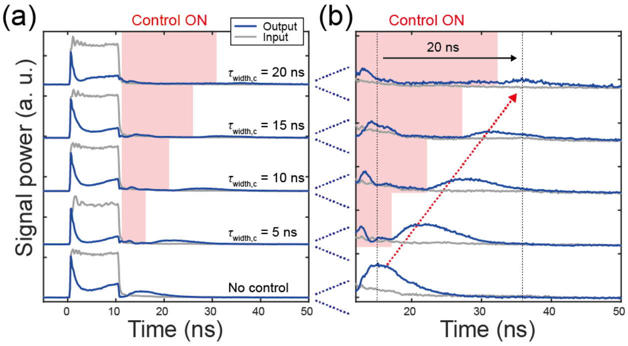


Fig 3 Experimental results for all-optical tunable buffering. (a) Signal outputs for different control pulse widths. The blue and gray solid lines represent the signal output and input, respectively. The time width of the input signal pulse is 10 ns. The pulse widths and the peak powers of the control pulses ($\tau_{\mathrm{width,c}}$, $P_{\mathrm{in,c}}$) are (5 ns, 15.1 W), (10 ns, 13 W), (15 ns, 8.4 W), and (20 ns, 7.3 W), respectively. The control pulse is inputted in the red region. (b) Enlargement of (a).

## 5. Conclusion

We have described an experimental demonstration of all-optical tunable buffering with coupled ultra-high $Q$ microcavities. The use of the Kerr effect made it possible to achieve all-optical tunable buffering with coupled ultra-high $Q$ WGM microcavities. We chose a silica toroid microcavity as the platform for our experiments because it has an ultra-high $Q$ factor (> 2 x $10^7$) and a small mode volume, and can be fabricated on a chip. Thanks to the ultra-high $Q$ factor and the Kerr effect, the maximum buffering time reached 20 ns, which was limited to a few hundred ps in previous studies.

## References

[1] Fleischhauer, M., Imamoglu, A. & Marangos, Rev. Mod. Phys. **77**, 633–673 (2005).
[2] Smith, D., Chang, H., Fuller, K., Rosenberger, A. & Boyd, R. Phys. Rev. A **69**, 063804 (2004).
[3] Xu, Q. et al. Phys. Rev. Lett. **96**, 123901 (2006).
[4] Yanik, M. & Fan, S. Phys. Rev. A **71**, 013803 (2005).
[5] Xu, Q., Dong, P. & Lipson, M. Nat. Phys. **3**, 406–410 (2007).
[6] Zheng, C. et al. Opt. Express **20**, 18319–18325 (2012).
[7] Armani, D., Min, B., Martin, A. & Vahala, K. J. Appl. Phys. Lett. **85**, 5439–5441 (2004).
[8] Ilchenko, V. et al. Opt. Commun. **145**, 86–90 (1998).
[9] Yoshiki, W. et al., *Preparing for submission*.
[10] Armani, D., Kippenberg, T., Spillane, S. & Vahala, K. Nature **421**, 925–928 (2003).
[11] Upham, J. et al. Opt. Express **21**, 3809–3817 (2013).

[12] Kondo, K. et al. Phys. Rev. Lett. **110**, 053902 (2013).

# Brillouin lasing in coupled silica toroid microcavities

Yoshihiro Honda (B4) Wataru Yoshiki (D3) Tomohiro Tetsumoto (D2) Shun Fujii (M1)

We achieved the 11 GHz mode splitting of supermodes that matched the Brillouin frequency shift in silica and realized the first observation of stimulated Brillouin scattering in coupled silica toroid microcavities.

**Key words:** Stimulated Brillouin scattering; Coupled microcavity; Toroid cavity;

## 1. Introduction

Stimulated Brillouin scattering (SBS) is a well-known nonlinear process in which two optical waves interact via an acoustic wave. The acoustic wave is generated via the electrostriction process. SBS in optical fiber, chip-based waveguides and microcavities has received a lot of attention because it can be employed for low-noise lasers, microwave synthesizers, slowing light and light storage. Whispering-gallery mode (WGM) microcavities with high $Q$ factors and small mode volumes enable us to generate SBS with a low threshold power. In this research, it is necessary to match the free spectral range (FSR) to the Brillouin frequency shift (tens of GHz) by using mm-scale cavities or to prepare high-order transverse WGMs that separate the Brillouin frequency shift to generate SBS [1-3]. With these approaches, it is very difficult to fabricate microcavities for SBS because we need to control the size of the microcavities precisely or to fabricate microcavities that have two optical modes that separate the Brillouin frequency shift.

Here we explore coupled microcavities to enhance the SBS effect. When two cavities are placed close together their optical modes are turned into supermodes such as symmetric and anti-symmetric modes. The coupled cavities enable mode separation to be freely tuned, and this allows us to avoid the need for precise control of the cavity size. In our study, we formed coupled microcavities by using a silica toroid microcavity, which has an ultra-high $Q$ factor and a small mode volume and can be fabricated on a chip. Although several studies have reported the development of coupled microcavities based on silica toroid microcavities, supermode splitting is limited to a few GHz [4]. If we can expand the splitting, we can employ coupled microcavities for various applications including stimulated Brillouin scattering (SBS).

In this paper, we report mode splitting of over 10 GHz using silica toroid microcavities. The optimization of the cavity geometry enables us to achieve supermode splitting exceeding 10 GHz. In addition, , we show the results of SBS experiments as an application of the large mode splitting. First, we simulate the splitting of the supermodes in coupled silica toroid microcavities and investigate the effect of cavity geometry on supermode formation. Second, we fabricate and characterize PMs based on silica toroid microcavities. Third, we perform SBS experiments. And we finish with a summary.

## 2. Calculation of coupling coefficient

Supermode splitting is quantified by using the coupling coefficient between the two microcavities that form a supermode. The calculation of the coupling coefficient between a tapered optical fiber and a microsphere has been reported [5]. We extend this method to coupled microcavities. The coupling coefficient between cavity1 (C1) and cavity2 (C2) is determined by the overlap between the profiles of the optical modes in the microcavities, and the phase matching condition. Taking these conditions into consideration, the coupling coefficient $\tilde{\kappa}_{C1,C2}$ can be written as

$$\tilde{\kappa}_{C1,C2} = \frac{\omega\varepsilon_0}{4}\left(n^2 - n_0^2\right) \times N_{C1}N_{C2}\iiint_{V_c}\left(E_{C1}(x,y,z) \cdot E_{C2}(x,y,z)\right)e^{i\Delta\beta z}dxdydz \quad (1)$$

where $n$ and $n_0$ are the refractive index of a silica toroid microcavity and air, $Vc$ is the cavity volume, $E_{C1}$ and $E_{C2}$ are the electrical fields of the two cavities, and $\Delta\beta$ is the propagation constant difference. Note that $N_{C1}$ and $N_{C2}$ are normalizing coefficients. The profile of the optical mode in each cavity is calculated by the finite element method (COMSOL Multiphysics [6]). Here we assume the fundamental modes. The splitting of the supermodes $\Omega$ can be written as

$$\Omega \approx \frac{c}{2\pi nR}\left|\tilde{\kappa}_{C1,C2}\right|^2. \quad (2)$$

In this simulation, we assumed microcavity diameters $R$ of 45, 55 and 65 µm. According to Fig. 1, the splitting of the supermodes is larger if we assume a microcavity with a smaller diameter. Moreover, this graph suggests that it is possible to obtain supermodes with a split of more than 10 GHz when 55-µm-diameter microcavities are used.

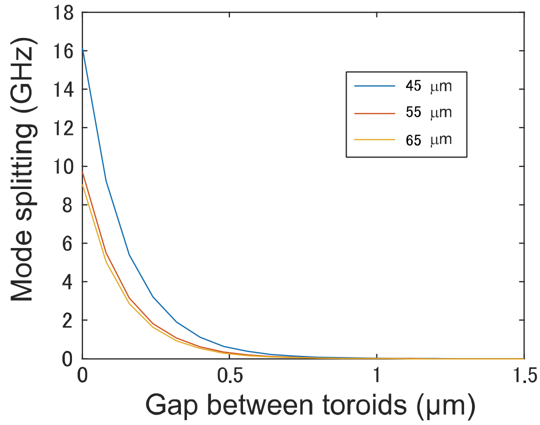


Fig. 1. Simulation results showing supermode splitting as a function of the gap between silica toroids.

## 3. Fabrication

We fabricated the silica toroid microcavities using photolithography, $XeF_2$ dry etching and $CO_2$ laser reflow. We fabricated the microcavities with a diameter of about 55 μm to achieve a split exceeding 10 GHz. As shown in Fig. 2(a), the coupled cavity system consists of two directly coupled silica toroids (C1 and C2), and a tapered optical fiber. PMs need two optical modes with the same frequency. Before coupling the two silica toroids, we selected two modes that were close to each other in frequency in each toroid. The temperature of C2 was controlled, and the resonance frequency of C2 matched the resonance frequency of C1. Under this condition, we moved C2 closer to C1 100 nm at a time. Figure 2(a) shows the transmission spectra for the different gaps between the two silica toroid microcavities. The coupling becomes stronger as the gap decreases because the overlap between the modes in the two cavities becomes larger. As predicted, the mode split is larger for a smaller gap. As shown in Fig. 2(b), we were able to obtain a mode split of about 11 GHz when the two toroids were placed closest together. At that time, the $Q$ factors of the supermodes were about $2 \times 10^6$. The experimental results were in good agreement with the simulation results. However, unlike in the simulation, we do not necessarily use the fundamental modes in the experiments. So in future research we will investigate the way in which the mode splitting changes depending on the optical modes used.

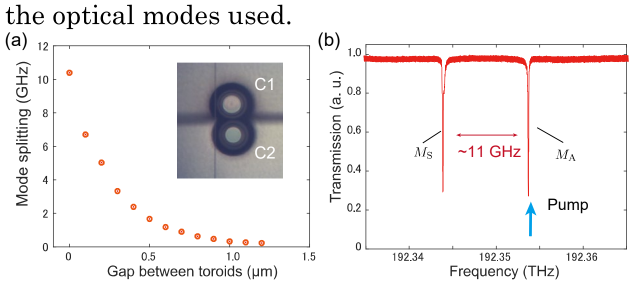


Fig. 2. (a) Mode split for different gaps between two cavities. Inset: microscope image of coupled silica toroid microcavities. (b) Measured transmission spectra of PM. ($M_S$: symmetric mode, $M_A$: anti-symmetric mode)

## 4. SBS experiment

We performed experiments on the SBS in the coupled cavities. Figure 3(a) shows the experimental setup. We used an optical circulator to detect the backward SBS light. In this experiment, the pump frequency matched the frequency of [???] *(Note: Something is missing here.)* (see Fig. 2(b)). The optical spectrum in the backward scattering light is shown in Fig. 3(b). There are two peaks in the optical spectrum. The right peak represents the Rayleigh scattering, and the left peak represents the SBS. In our experiment, we achieved a threshold power of about 50 mW (Fig. 3(c)). This threshold power should be further reduced by optimizing the coupling condition and the cavity geometry.

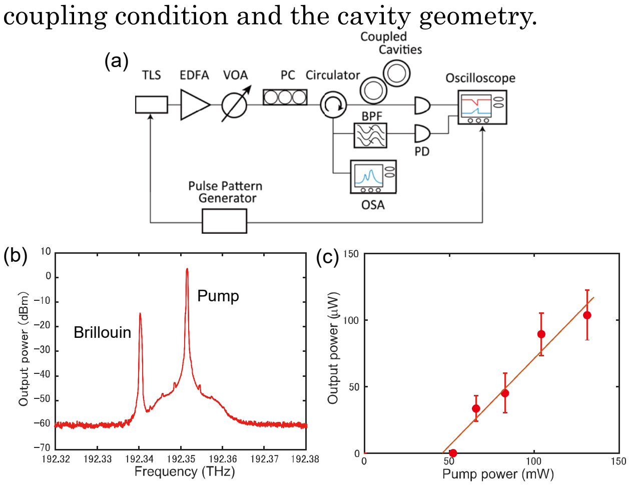


Fig. 3. (a) Experimental setup for Brillouin lasing. (b) Optical spectrum of the backscattering light. The pump signal is on the right and the SBS light is on the left. (c) SBS output power for different pump input powers.

## 5. Conclusion

We reported supermode splitting of over 10 GHz using silica toroid microcavities. Our simulation suggested that larger mode splitting is possible if we use silica toroid microcavities with a smaller diameter. We fabricated silica toroid microcavities with a diameter of about 55 μm and achieved the 11 GHz mode splitting of supermodes, which matches the Brillouin frequency shift in the silica in coupled silica toroid microcavities. The large mode splitting enabled us to perform the SBS experiment.

## References

[1] I. S. Grudinin, A. B. Matsko, and L. Maleki, Phys. Rev. Lett. **102**, 043902 (2009).

[2] H. Lee, T. Chen, J. Li, K. Y. Yang, S. Jeon, O. Painter, and K. J. Vahala, Nat. Photonics **6**, 369–373 (2012).

[3] G. Lin, S. Diallo, K. Saleh, R. Martinenghi,

J.-C. Beugnot, T. Sylvestre, and Y. K. Chembo, Appl. Phys. Lett. **105**, 231103(2014).
[4] I. S. Grudinin, H. Lee, O. Painter, and K. J. Vahala, Phys. Rev. Lett. **104**, 083901 (2010).
[5] M. J. Humphrey, E. Dale, A. T. Rosenberger, and D. K. Bandy, Opt. Commun. **271**, 124–131 (2007).
[6] M. Oxborrow, IEEE Trans. Microw. Theory Tech. **55**, 1209–1218 (2007).

# Ammonia gas detection with high sensitivity using a silica toroid microcavity

Misako Kobayashi (M2)

An ordinary silica toroid microcavity is insensitive to ammonia gas. However, in this study, I successfully detect ammonia gas by using a silica toroid microcavity with bilayers of polyelectrolyte, and I obtain a higher detection sensitivity and higher detection resolution than any previously reported ammonia gas sensor.

**Key words:** Silica toroid microcavity; Ammonia gas; Sensing

## 1. Introduction

The performance of measuring instruments is making continuous progress and the size of objects that can be measured has become smaller and smaller. However, the effect of background noise cannot be ignored because smaller objects for measurement generate smaller signals. To solve this problem, optical cavities are used. Optical cavities can amplify a specific signal, and the signals from the object can be distinguished from other signals. Moreover, optical cavities enable light to interact with the object more than once, and the size of measuring instrument becomes smaller. The performance of optical cavities is decided by the $Q$-factor and $V$. The $Q$-factor indicates the signal confinement time in cavities, and $V$ indicates the signal confinement volume, and so optical cavities with a high $Q$-factor and a low $V$ are superior. Among optical cavities, the optical microsphere, which was fabricated by L. Collot *et al.* in 1993 [1], has attracted a great deal of attention because it has a high $Q$-factor and a low $V$, and can be fabricated easily. In addition, a silica toroid microcavity was fabricated by D. K. Armani *et al.* in 2003 [2]. A silica toroid microcavity has a lower $Q$-factor but a smaller $V$ than a microsphere and can be fabricated on a chip [3]. For that reason, silica toroid microcavities are used in various fields including research on the development of a high sensitivity sensor. However, cavities and waveguides are difficult to accumulate and research on the practical realization of a high sensitivity sensor has shown little progress.

In this study, my aim was to detect ammonia gas with high sensitivity by using a silica toroid microcavity and a tapered fiber that were aligned on resonance.

## 2. Deposition of bilayers

It is known that the shrinkage of a polyelectrolyte bilayer depends on the condition of the polyelectrolyte ion [4]. Bilayers of polyelectrolyte are deposited by electrostatic self-assembly (ESA). In this study, I deposited bilayers of poly(acrylic acid)(PAA) and poly(allylamine hydrochloride)(PAH), which have various uses including as fundamental films, sensors and nanomaterials. The deposition procedure is described below.

1. Fabricate a silica toroid microcavity.
2. Use sodium chloride to prepare PAA solution and PAH solution whose pH values are around 7.0.
3. Clean the toroid microcavity with piranha solution for 4 minutes. Piranha solution is $H_2SO_4 : H_2O_2 = 7 : 3$.
4. Clean the cavity with ultrapure water for 5 minutes.
5. Dry the cavity with $N_2$ gas.
6. Soak the cavity in PAH solution for 4 minutes.
7. Clean the cavity with ultrapure water for 1 minute.
8. Soak the cavity in PAA solution for 4 minutes.
9. Clean the cavity with ultrapure water for 1 minute.
10. Repeat steps 6-9 of the process and form 20 or 30 bilayers in the cavity.
11. Bake the cavity in an oven at 60℃ for 2 hours.

I purchased PAH solution and PAA solution from SIGMA-ALDRICH and diluted them with pure water with 3.3 mM PAH solution and 2.4 mM PAA solution. Although the surface of an ordinary silica toroid microcavity has a neutral charge, it becomes negative as a result of steps 3-5 above. Under this condition, soaking a toroid microcavity in PAH, which becomes a cation in solution, and PAA, which becomes an anion in solution, provides bilayers as a result of Coulomb force. Figure 1(a) shows a photograph taken before bilayer deposition, and Fig. 1(b) and (c) show photographs taken after the deposition of 20 or 30 bilayers. From Fig. 1(a) and (b), because of the 20 PAA/PAH bilayers, the surface of the silica toroid microcavity has hardly changed although the $Q$-factor decreased from $Q = 6.2\times10^6$ (before deposition) to $Q = 1.2\times10^6$(after deposition). On the other hand, from Fig. 1(a) and (c) the surface of a silica toroid microcavity became white after the deposition of 30 PAA/PAH bilayers., The $Q$-factor of the cavity could not be measured under this condition.

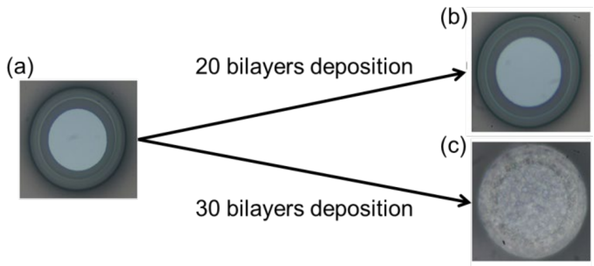


Fig 1 : Photographs of a silica toroid microcavity. (a) Before bilayer deposition, (b) after deposition of 20 PAA/PAH bilayers, and (c) after deposition of 30 PAA/PAH bilayers.

### 3. Construction of experimental system with gas

Ammonia gas is a poisonous and combustible gas, and causes the irritation and corrosion of human skin and mucous membranes. Therefore, I constructed the measuring system shown in Fig. 2 paying attention to safety and ease of handling.

A PD-1B permeater (purchased from GASTEC) is used as a gas generator. The gas source of the permeater is a permeation tube consisting of a sealed fluorine resin tube containing highly pure liquefied gas. A trace concentration of the calibration gas can be continuously prepared by maintaining the permeation tube at a constant temperature and supplying a specific quantity of dilution gas. In this way, the calibration gas concentration can be defined by calculating the weight loss of the permeation tube and the amount of dilution gas. And highly reactive gas such as ammonia gas can be prepared because the approach consists of dynamic adjustment. Gas generated in the permeater flows into a package containin a silica toroid microcavity and a tapered fiber with Teflon or nylon gas piping, and ammonia gas detection is performed. The procedure with the packaged cavity is shown in Fig. 3. First, approximately 0.1 mL UV curable polymer is applied to silicon chips on both sides of a silica toroid microcavity (a). Then, the cavity and tapered fiber are aligned on resonance by viewing them from the top and side (b), and UV light is irradiated for 20 minutes. The ammonia gas is removed by using zeolite, which is an adsorbent of ammonia gas, and the packaged cavity is placed under a fume hood. This procedure prevents ammonia gas from leaking into the outside environment.

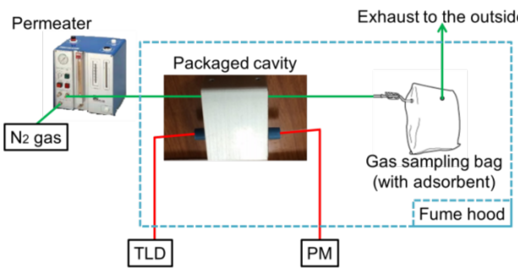


Fig. 2: Experimental setup for ammonia gas detection. Green lines indicate gas piping and red lines indicate optical patch cable.

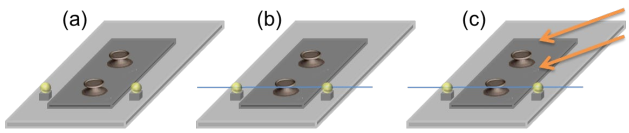


Fig. 3: Schematics of the packaging procedure for a silica toroid microcavity and tapered fiber. (a) Apply approximately 0.1 mL UV curable polymer on silicon chips to both sides of the cavity. (b) Align the cavity and tapered fiber on resonance. (c) Irradiate UV light for 20 minutes.

### 4. Ammonia gas detection

Ammonia gas detection was performed by using the experimental system shown in Fig. 2 and a silica toroid microcavity with 20 PAA/PAH bilayers. When a sensing experiment is performed with microcavities, the observation of the shift of wavelength shift plays major role, and in this study, I used this approach. In this way, the factors that determine the detection sensitivity are (1) the $Q$ factor of a silica toroid microcavity, (2) the fluctuation of the light source and (3) the temperature change induced by the ammonia gas flow. In this study, (2) and (3) may become problems. I use a tunable laser TSL-710 (SANTEC) as a light source. Because its wavelength accuracy measured by using packaged cavity is 0.01 pm, the effect of light source fluctuation can be ignored when the packaged cavity is used. Therefore, I constructed the experimental setup shown in Fig. 4. Two packaged cavities are prepared and 20 PAA/PAH bilayers are deposited on one of them. The two cavities are connected in series and the cavity with PAA/PAH bilayers is used as a sensor cavity and the other ordinary cavity is used as a reference cavity. By connecting the two cavities in series, dips derived from each cavity can be observed as in Fig. 5. The pink arrow in Fig. 5 shows the resonant wavelength derived from the sensor cavity, and the orange arrow shows the resonant wavelength derived from the reference cavity. The $Q$ factor of the sensor cavity was $Q = 7.5\times10^5$, and the $Q$ factor of the reference cavity was $Q = 2.0\times10^5$.

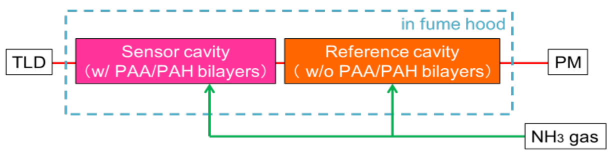


Fig. 4: Experimental setup for ammonia gas detection using a silica toroid microcavity.

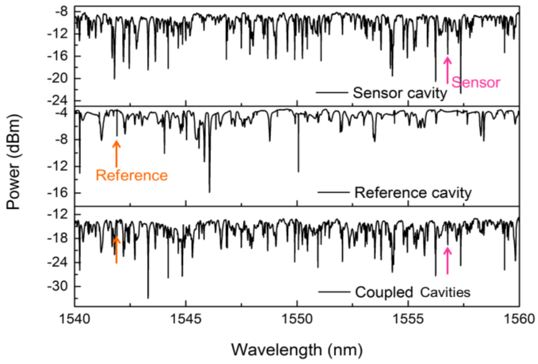

Fig. 5: Transmittance spectrum of sensor cavity (top), reference cavity (middle), and both cavities (bottom).

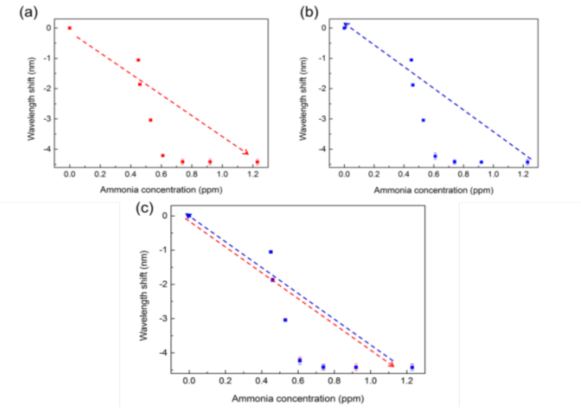

Fig. 6: Comparison between packed cavity and unpacked cavity (a) without vibration (b) with vibration. (c) differences between (a) and (b).

Ammonia gas was detected by observing the two resonant wavelength shifts, and the result is shown in Fig. 6. Figure 6(a) shows the wavelength shift when the ammonia gas concentration was increased from 0 to 1.23 ppm, Figure 6(b) shows the wavelength shift when the ammonia gas concentration was decreased from 1.23 to 0 ppm, and Fig. 6(c) is a superposition of Fig. 6(a) and Fig. 6(b). From Fig. 6(c), the relationship between the ammonia gas concentration and the wavelength shift is almost the same whether increasing or decreasing the ammonia gas concentration. The average error rate of each ammonia gas concentration is $4.96 \times 10^{-4}$ %, and this result indicates that the ammonia gas sensor fabricated in this study has sufficient reversibility. In addition, I evaluated the fabricated sensor by defining detection sensitivity as the minimum ammonia gas concentration required for detection, and the detection resolution is the value obtained with the following equation (4.1).

$$\text{Detection resolution} = \frac{\text{Wavelength fluctuation}}{(\text{Detection sensitivity})(Q\text{−factor})} \quad (4.1)$$

From these definitions, the fabricated cavity has a 450 ppb detection sensitivity, which is limited by the permeater and the 1.67 ppb detection resolution. Table 1 compares the fabricated sensor and other sensors such as the FEC44-100(FIGARO Engineering) [5], graphene sensor [6], and optical fiber with PAA/PAH bilayers [7]. Table 1 reveals that both the detection sensitivity and detection resolution of the fabricated sensor are superior to those of other ammonia gas sensors.

Table 1 : Comparison of various ammonia gas sensors

| Type of sensor | Detection sensitivity | Detection resolution |
|---|---|---|
| Semiconductor[5] | 1 ppm | 1 ppm |
| Graphene[6] | 2 ppm | 200 ppb |
| Optical fiber[7] | 20 ppm | - |
| Silica toroid microcavity | 450 ppb | 1.67 ppb |

## Summary

A silica toroid microcavity with 20 PAA/PAH bilayers can be used for ammonia gas detection and can provide higher detection sensitivity and higher detection resolution than other types of ammonia gas sensors. The $Q$ factor of the silica toroid microcavity used in this study was not high, and so the fabrication of a more highly sensitive ammonia gas sensor can be expected by using a silica toroid microcavity with a higher $Q$ factor.

## References


[1] L. Collot, V. Lefevre-Seguin, M. Brune, J. M. Raimond and S. Haroche, "Very high-Q whispering-gallery mode resonances observed on fused silica microspheres," Europhys. Lett. **23**, 327-334 (1993).

[2] D.K. Armani, T. J. Kippenberg, S. M. Spillane and K. J. Vahala, "Ultra-high-Q toroid microcavity on a chip," Nature **421**, 925-927 (2003).

[3] K. J. Vahala, "Optical microcavities," Nature **424**, 839-846 (2003).

[4] S. S. Shiratori and M. F. Rubner, "pH-dependent thickness behavior of sequentially adsorbed layers of weak polyelectrolytes," Macromolecules **33**, 4213-4219 (2000).

[5] http://www.figaro.co.jp/product/entry/fecs44-100.html

[6] S. M. M. Zanjani, M. M. Sadeghi, M. Holt, F. Chowdhury, L. Tao, D. Akinwande, "Enhanced sensitivity of graphene ammonia gas sensors using molecular doping," Appl. Phys. Lett. 108, 033106 (2016).

[7] X. Huang, X. Li, H. Chen, X. Che, and J. Yang," Thin-core fiber modal interferometer for ammonia sensing, " Asia Pacific Optical Sensors Conference, W4A.19, Shanghai China, October 11-14(2016).

# Immobilization of bovine serum albumin in a silica toroid microcavity

Taku Okamura (B4) Misako Kobayashi (M2)

Sensors are tools used to obtain various types of information about neighboring environments, for example the kind and density of molecules, atmospheric pressure, and temperature. A biosensor is used for medical tests, and represents a very important technique. A protein sensor, which is a type of biosensor, has already been used for certain kinds of medical examination, but thus far an examination designed to detect an ideal biomarker has yet to be realized. Therefore, we tried sensing bovine serum albumin with a micro optical resonant sensor, which attracted attention in recent years for a number of reasons.

**Key words**: Silica toroid microcavity; Sensing, Bovine serum albumin; Surface treatment

## 1. Introduction

An optical cavity is an element that can confine light for a very long time. The interaction between light and a given material becomes stronger by confining light with an extremely high density in the small domain of this optical microcavity, and it is believed that this will lead to the development of all-light switches and highly sensitive optical sensors.

In particular, an optical microcavity can confine light in a very small space for a long time, and so can cause a strong interaction between light and material when the light intensity is weak or the device is small. Therefore, it has been reported that it is possible to fabricate a small and sensitive sensor [1].

In this study we used a surface treatment to enable a silica toroid microcavity, whose performance is particularly good among microcavities, to immobilize a protein. We then attempted to detect the protein, which was immobilized on the microcavity surface.

## 2. Bovine serum albumin

Because serum albumin is seen clearly in blood, and can be easily refined, it is one of the first proteins to be studied by scientists. Bovine serum albumin (BSA), which is a similar protein obtained from cows, is used when a standard protein must be studied. Therefore, for this study we chose bovine serum albumin for detection by the silica toroid microcavity.

## 3. Film formation by surface treatment

The silica used for the silica toroid microcavity is an inorganic material, and it is necessary to perform a surface treatment because the reactivity between organic matter such as proteins and the microcavity is poor [2]. Specifically, is the treatment consists of employing 1. piranha cleaning, 2. An amino group functionalized with a silane coupling agent, and 3. An aldehyde group functionalized with glutaraldehyde. The amino group of the side chain of the protein and the aldehyde group of the microcavity surface induce a reaction and solidify because their cross-linkage advances. In this way, the silica surface of the microcavity can immobilize protein. Below, we detail the surface treatment procedure.

1. Clean a toroid microcavity with piranha solution for 4 minutes. Piranha solution is $H_2SO_4 : H_2O_2 = 3 : 1$.
2. Clean the toroid microcavity with pure water for 5 minutes.
3. Dry the toroid microcavity with $N_2$ gas.
4. Soak the toroid microcavity in APTES (3-Aminopropyl) triethoxysilane) for 2 hours.
5. Clean the toroid microcavity with ethanol for 1 minute.
6. Clean the toroid microcavity with pure water for 1 minute.
7. Heat the toroid microcavity with a hot plate at 90 °C for 1 hour.
8. Soak the toroid microcavity in glutaraldehyde for 1 hour.
9. Clean the toroid microcavity with ethanol for 1 minute.
10. Clean the toroid microcavity with pure water for 1 minute.

Figure 1 shows photographs of the silica toroid microcavity before and after each part of the surface treatment.

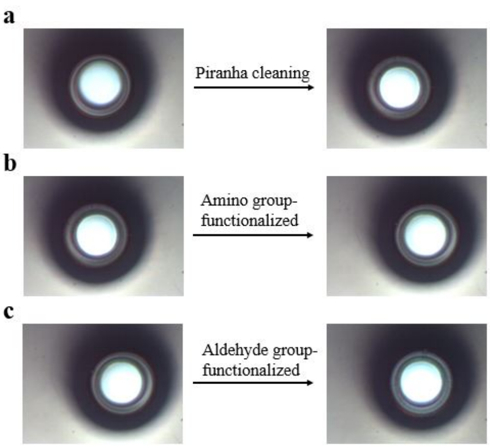


Fig. 1: Photographs of a silica toroid microcavity. (a) Before surface treatment and after piranha cleaning (b)After piranha cleaning and after amino group functionalization. (c) After amino group functionalization and after aldehyde group functionalization.

## 4. Performance evaluation of microcavity before and after surface treatment

A cavity is an element that confines light, and quality factor is used as a universal standard for this property. The quality factor expresses the light confinement duration and is an important parameter when evaluating the performance of the optical microcavity along with mode volume, which expresses the amount of light confined in a small volume. The large quality factor shows that the light confinement effect is efficient, and the small mode volume shows that the power density of the cavity is high.

We measured the quality factor before and after surface treatment to allow us to evaluate the performance of the microcavity. As a result, we obtained $Q = 2.4\times10^6$ before surface treatment and $Q = 4.2\times10^5$ after treatment.

## 5. Sensing experiment

We used the microcavity sensor to observe the refractive index change in neighboring media as a resonance wavelength change. In other words, the resonance wavelength shifts when a protein particle attaches to the cavity surface. In this study, we attempted to detect bovine serum albumin using this phenomenon.

We fixed the cavity with the treated surface on a pool filled with MES(2-Morpholinoethanesulfonic acid) buffer solution. We injected 1μM of BSA and observed the shift in the resonance wavelength. We placed a resonator in the MES buffer solution because we wanted to prevent the protein from changing under the influence of the pH. We used a laser operating in a visible light band because the light absorption of water is its smallest in the visible light region.

We show an experimental result in Fig. 2. We found that the resonance wavelength shifted to the long wavelength side before and after BSA injection.

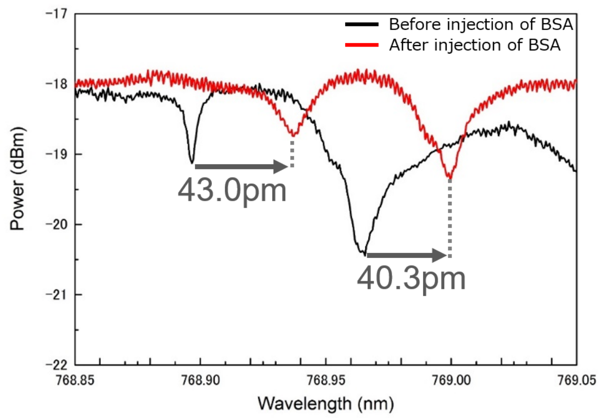


Fig. 2: Wavelength shift before and after injection of BSA. The black and red lines show transmissions before and after BSA injection, respectively.

In Fig. 3, we show a graph that expresses the relationship between the amount of wavelength shift and the time after the BSA injection. The resonance wavelength shift becomes large over time after BSA injection and then saturates.

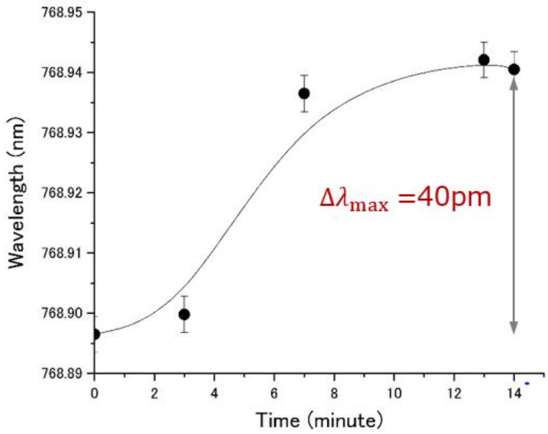


Fig. 3: Relationship between amount of wavelength shift and time after BSA injection.

Using the obtained wavelength shift, we found that the sensitivity became 1.5 nM when roughly estimated from reference [3]. This is around one-tenth that of a previous study. This is because the quality factor was around $Q = 10^6$ in the earlier study, whereas in this study it was around $Q = 10^5$. In other words, we believe this to be because of the difference in the Q level of the cavity.

## 6. Summary

We treated the surface of a silica toroid microcavity and immobilized bovine serum albumin on it. In addition, we performed a light sensing experiment on the immobilized bovine serum albumin and observed a long wavelength shift of approximately 40 pm. The roughly estimated sensitivity is not superior to that of a previous study, but we can expect the sensitivity to be improved by raising the Q level peculiar to a cavity.

## References

[1] Andrea M. Armani, et al., Science, 317, 783 (2007)
[2] Shota Kita, et al., Optics express, 19, 17683 (2011)
[3] Frank Vollmer, and Stephen Arnold, Nature Methods, 5, 591 (2008)

# Mode interaction via stimulated Raman scattering in a silica toroid microcavity

Takumi Kato(D3), Atsuhiro Hori(M1), Ryo Suzuki(D1), Shun Fujii(M1)

Stimulated Raman scattering in a silica toroid microcavity is often observed with high power pumping. Silica has a broad Raman gain because of its amorphous structure and this induces multi-mode Raman oscillation. This report describes the mode interaction via stimulated Raman scattering in a silica toroid microcavity. We focus on two patterns: Raman oscillation in the same and in different mode families. A mathematical approach shows that mode overlapping and the ratio of quality factors determines whether or not mode interaction occurs. Experiments and numerical simulations agree well with the mathematical [insight/results?].

**Key words** : Silica toroid microcavity, Kerr comb, Raman comb, mode interaction, Lugiato-Lefever equation

## 1. Background

Kerr comb generation with a high-$Q$ microcavity has been studied intensively over the past decade. A silica toroid microcavity is one of the microcavities used for Kerr comb generation; it requires a high optical density to induce four-wave mixing from a continuous-wave pump. On the other hand, stimulated Raman scattering is still an attractive way to achieve wavelength-conversion. In 2002, Raman lasing with a silica whispering microsphere was reported. Multi-mode lasing is often observed thanks to the broad Raman gain in silica. In this research, we focus on multi-mode lasing via stimulated Raman scattering in a silica toroid microcavity.

The maximum Raman gain in silica is at a distance of 500 cm$^{-1}$ from the pump. The full-width at half-maximum of the Raman gain is 260 cm$^{-1}$. For example, when the pump wavelength is 1550 nm, the maximum gain is around 1655 nm and the FWHM is in the 1620 – 1680 nm range. Thus, multi-mode lasing (Raman comb) is often observed. A broad Raman comb covering 1500 – 2200 nm can be achieved. On the other hand, mode interaction often occurs, and Raman oscillation in a different mode family is observed. The purpose of this report is to understand the mode interaction via stimulated Raman scattering.

## 2. Threshold power of stimulated Raman scattering

Here, stimulated Raman scattering is described in detail. The threshold of stimulated Raman scattering in a silica toroid microcavity is described as follows [3]:

$$P_{\mathrm{th}} = \frac{\pi^2 n^2 V_{\mathrm{eff}}}{\lambda_p \lambda_R g_R} Q_e^P \left(\frac{1}{Q_T^P}\right)^2 \frac{1}{Q_T^R} \qquad (1)$$

where $n, V_{\mathrm{eff}}, \lambda_P, \lambda_R,$ and $g_{\mathrm{R}}$ are the refractive index, the effective mode volume, the wavelength of the pump mode, the wavelength of the Raman mode, and the Raman gain, respectively. $Q_{\mathrm{e}}^P, Q_T^P,$ and $Q_T^R$ are the coupling $Q$ of the pump mode, the total $Q$ of the pump mode, and the total $Q$ of the Raman mode, respectively.

The effective mode volume is described as follows:

$$V_{\mathrm{eff}} = \frac{\int |E_p|^2 dV \int |E_R|^2 dV}{\int |E_p|^2 |E_R|^2 dV} \qquad (2)$$

Generally, the Raman oscillation occurs in the same mode family as the pump mode. In contrast, we focus on whether the Raman oscillation in a different mode family occurs in a silica toroid microcavity. The threshold power of both oscillations is compared. The silica toroid microcavity with a major diameter of 100 μm and a minor diameter of 8 μm is considered. We considered three optical modes ($TE_{00}$, $TE_{01}$, $TE_{10}$). The effective mode areas are calculated with COMSOL and are given as $V_{\mathrm{eff}} = 2\pi r \times A_{\mathrm{eff}}$, where $r$ is the radius of a cavity. The calculated mode areas are $A_{\mathrm{eff\ TE00\text{-}TE00}} = 9.75$ μm$^2$, $A_{\mathrm{eff\ TE01\text{-}TE01}} = 12.79$ μm$^2$, $A_{\mathrm{eff\ TE02\text{-}TE02}} = 17.75$ μm$^2$, $A_{\mathrm{eff\ TE00\text{-}TE01}} = 18.19$ μm$^2$, $A_{\mathrm{eff\ TE00\text{-}TE10}} = 21.69$ μm$^2$, $A_{\mathrm{eff\ TE01\text{-}TE10}} = 29.45$ μm$^2$. To compare the ratios of different excited transverse mode families via the SRS process, we define the power ratio $C$ as,

$$C = \frac{P_{\mathrm{th\_same}}}{P_{\mathrm{th\_diff}}} = \frac{A_{\mathrm{eff\_same}}}{A_{\mathrm{eff\_diff}}} \frac{Q_{T\mathrm{\_diff}}}{Q_{T\mathrm{\_same}}} \qquad (3)$$

where, $P_{\mathrm{th\_same}}$ and $P_{\mathrm{th\_diff}}$, $A_{\mathrm{eff\_same}}$ and $A_{\mathrm{eff\_diff}}$, $Q_{\mathrm{T\_same}}$ and $Q_{\mathrm{T\_diff}}$ are the SRS threshold powers, effective mode areas, and total $Q$s of the Raman mode, respectively. The subscript indicates whether the Raman mode is in the same or a different mode family. When $C$ is higher than 1, the SRS threshold power of a Raman mode in a different mode family is lower than that for one in the same mode family, which means that the SRS to the different mode family will be dominant. Figure 1(b) shows the calculated $C$ value as a function of $Q_{\mathrm{T\_diff}}/Q_{\mathrm{T\_same}}$ for three different mode combinations. The blue, red and black lines show the cases for $TE_{01}$(pump)-$TE_{00}$(different), $TE_{10}$(pump)-$TE_{00}$(different), and $TE_{10}$(pump)- $TE_{01}$(different), respectively. Since the $Q$ of a high-order mode is usually lower than that of a lower order mode, these three cases are sufficient to understand the influence of the mode interaction in the SRS. When $Q_{\mathrm{T\_diff}}/Q_{\mathrm{T\_diff}} < 1$, $C$ is smaller than 1 in all cases because the mode overlapping is not perfect. However, $C$ is larger than 1 in three cases when $Q_{\mathrm{T\_diff}}/Q_{\mathrm{T\_same}} > 2$. This suggests that a mode interaction will occur easily when the $Q$ factor of one mode is only double that of the pump mode. Generally, the $Q$ factor of the fundamental mode ($TE_{00}$ mode) is much higher than that of a high-order mode (i.e. $TE_{01}$) in a silica toroidal microcavity.

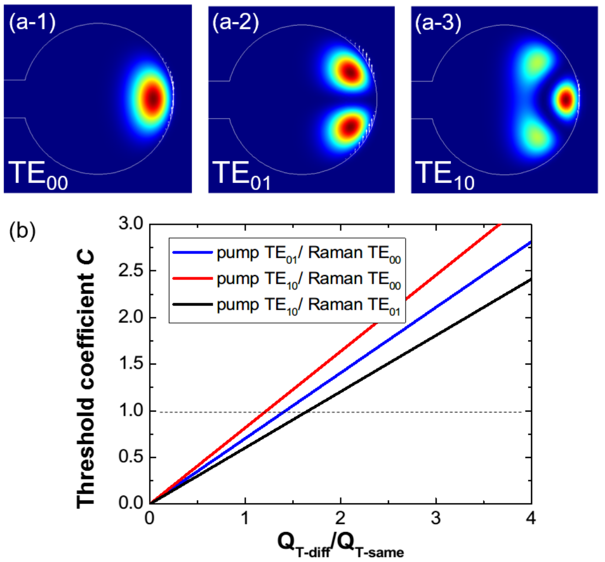


Fig. 1 (a) Cross-sectional mode profiles of a silica toroid microcavity. These results were obtained using the finite-element method (COMSOL Multiphysics). The diameter of the microcavity is 100 μm and the minor diameter is 8 μm. The results are for the $TE_{00}$, $TE_{01}$, and $TE_{10}$ modes. (b) Calculated threshold coefficient $C$. The blue, red, and black lines indicate combinations of $TE_{01}$(pump)-$TE_{00}$(Raman), $TE_{01}$ (pump)-$TE_{00}$ (Raman), and $TE_{10}$(pump)-$TE_{01}$ (Raman), respectively. The fact that the coefficient $C$ is greater than 1 means that the threshold of excitation for a different mode family is lower than that for the same mode family, indicating that a mode interaction should occur.

## 3. Mode interaction via stimulated Raman scattering

To confirm the theory, we conducted experiments with a silica toroidal microcavity. We pumped one of the modes and observed the spectrum as shown in Fig. 2(a). A comb spectrum ranging from 1400 to 2000 nm was obtained. Figure 2(c) is a magnified view of Fig. 3(a), which shows that the SRS occurs in the same mode family as the pump mode. Then, we pumped the cavity in a different mode. The result is shown in Fig. 2(b), where we observe a dual-comb-like spectrum. The magnified view in Fig. 2(b) clearly shows that a different mode family is excited via the SRS process. Please note that the transverse mode is not generated through FWM because of the energy and momentum mismatch. The frequency difference between these two mode families is about 180 GHz. Next, we measured the $Q$s of the pump and the SRS comb modes. We performed a conventional transmittance spectrum measurement using a tunable wavelength sweep laser, and obtained $Q$s of $1.1 \times 10^7$ for the 1548.96 nm mode (H0 mode) and $3.1 \times 10^6$ for the 1543.08 nm mode (L0 mode), as shown in Figs. 3(a) and (b), respectively. The ratio $Q_H/Q_L$ is 3.5. This is a reasonable value with which to achieve mode interaction.

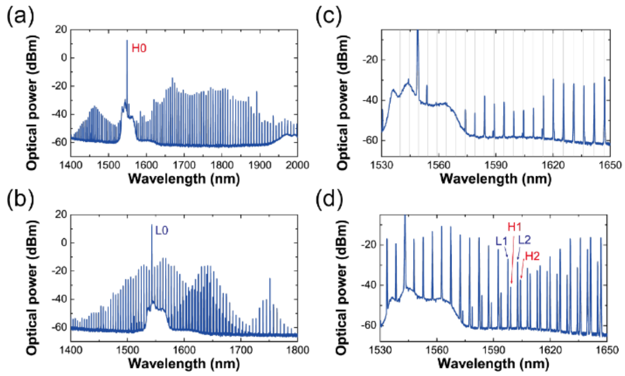


Fig. 2 Optical spectra pumped with different modes. The same cavity was used in every case. The graphs show the spectra when the pump wavelengths were (a) 1548.96 nm and (b) 1543.08 nm. The pump power was about 1 W after the EDFA. (c) and (d) are magnified views of (a) and (b), respectively. The equidistant vertical gray lines in (c) show that the SRS comb was generated in the same mode family as the pump mode

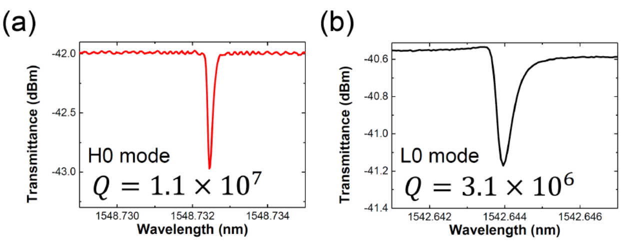


Fig. 3 (a) Transmittance spectrum for the 1548.96 nm mode used in Fig. 5.4(a). (b) Same as (a) but for 1543.08 nm. It should be noted that the resonance is at a shorter wavelength in Figs. 3(a) and (b) due to the presence of the thermo-optic effect, but we are measuring the same mode

## 4. Numerical simulation

We developed a numerical model to describe the behavior of a nonlinear cavity in which FWM and SRS occur simultaneously. To obtain a full understanding, we modified the LLE [4] and took the nonlinear energy transition via SRS into account [5]. To explain the experimental results, we adopted a pump mode with a $Q$ of $5.0 \times 10^6$. Based on the theoretical understanding, we used the $Q$ factor ratio, $Q_{\mathrm{Raman}}/Q_{\mathrm{pump}}$, as a parameter. Figure 4(a) shows the calculation results when $TE_{01}$ and

$TE_{00}$ are adopted as the pump and Raman modes, respectively. The vertical axis is the integrated light power of the generated SRS mode. Since each calculation time is tens of thousands of round trip times, the cavity is set in a steady state. When the $Q$ factor ratio is 2, the Raman power suddenly increases, which means that the gain overcomes the cavity loss. The value agrees with the theoretical prediction as discussed in section 2 and shown Fig. 4(b). Figure 4(c) shows the optical spectrum when the ratio is 3, which corresponds to our experimental values. The spectrum has the same shape as the experimental result shown in Fig. 2(b). On the other hand, when we pump at a higher mode, we obtain the spectrum shown in Fig. 4(d). The Raman power does not increase, and this is in good agreement with Fig. 2(a).

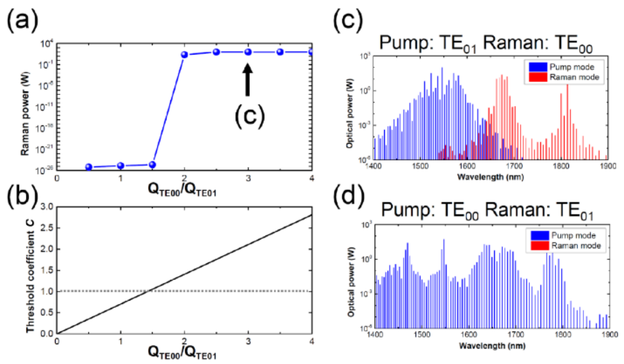


Fig. 4 Simulation results with the model we used in our experiments. The input power is set at 1 W. (a) Integrated power of SRS modes versus $Q_{\mathrm{TE00}}/Q_{\mathrm{TE01}}$. The $Q$ of the TE01 mode is defined as $5.0{\times}10^{6}$. As $Q_{\mathrm{TE00}}$ /$Q_{\mathrm{TE01}}$ increases and exceeds 2, the SRS mode power increases rapidly, because the gain exceeds the SRS threshold. (b) The theoretical threshold coefficient $C$ mentioned in section 2. (c) The optical spectrum when $Q_{\mathrm{TE00}}/Q_{\mathrm{TE01}}$ = 3. (d) High-$Q$ mode pumping with the same $Q$ ratio as (c). No transverse mode coupling was observed.

## 5. Summary

In this study, we focused on the transverse mode interaction via stimulated Raman scattering in a silica toroidal microcavity. We measured a twin comb spectrum experimentally and confirmed that the $Q$ values of the modes are key parameters as regards allowing the generation of combs in different mode families. The dual comb is only present when we pump in a low-$Q$ mode. The experimental results are in good agreement with the theoretical understanding when the critical point for the transverse mode interaction is present at a $Q$ ratio larger than two. We developed a numerical model based on LLE considering the mode interaction via Raman scattering and the spectra of the numerical and experimental results were the same.

## References

[1] T. Kippenberg, *et al*., Science **332,** 555-559 (2011).
[2] S. Spillane, *et. al*, Nature **415,** 621-623 (2002).
[3] T. J. Kippenberg, *et. al*, IEEE J. Sel. Top. Quantum Electron. **10,** 1219–1228 (2004).
[4] L. A. Lugiato and R. Lefever, Phys. Rev. Lett. **58,** 2209–2211 (1987).
[5] T. Kato *et al*., Opt. Express **25,** 857-866 (2017).

# Fabrication and characterization of silica rod microcavity

Akihiro Kubota(B4)

A whispering gallery mode (WGM) microcavity has a very high quality factor, and so it can confine light to a small volume for long periods of time. A silica rod microcavity is one type of WGM cavity, and it has high tolerance to optomechanical vibration. Hence, we can expect a silica rod microcavity to be used as a stable Kerr comb light source. In this research, we fabricated and characterized silica rod microcavities. We observed a third order nonlinear optical effect in silica rod microcavities.

**Key word**：Optical microcavity, Optical frequency comb, Third order nonlinear optical effect

## 1. Background

An optical frequency comb is an optical signal with many frequency components with equal line spacing [1]. An optical frequency comb is, for example, generated by using a mode locked laser such as a Ti:sapphire laser or a fiber laser. A technique for precise frequency measurement with an optical frequency comb was established by T. W. Hänsch of the Max Planck Institute of Quantum Optics (MPQ) and J. L. Hall of the Joint Institute for Laboratory Astrophysics (JILA). In 2005, they won the Nobel Prize in Physics for their contribution to developing precise metrology with a frequency comb.

Recently, optical frequency combs from a microcavity have attracted increased research interest. This type of optical frequency comb is called a Kerr comb. A Kerr comb is generated with a WGM microcavity, which has a high quality factor and can confine light in a small volume for long periods of time. In the microcavity, the interaction between light and matter is enhanced, and so various optical nonlinear effects can be generated efficiently. A Kerr comb is an optical frequency comb generated via cascaded four-wave mixing in a microcavity. A Kerr comb offers the potential for miniaturization, cost reduction, and saving energy [2,3].

## 2. Silica rod microcavity

The silica rod microcavity was proposed by P. Del'Haye of the National Institute of Standards and Technology (NIST) in 2013 [4]. A silica rod microcavity has a high quality factor and can be fabricated easily. The diameters of silica rod micro-cavities can be from a few hundred micrometers to a few millimeters. The free spectral range (FSR) of the cavity can be from a few GHz to a few hundred GHz. The diameter and FSR of silica rod micro-cavities can be changed over a wide range. Many microcavity applications have been proposed in previous research, for example coherent terabit communications [5], and an optoelectronic microwave oscillator [6]. In these applications, microcavities with an FSR in the few GHz to a few hundred GHz range are important.

## 3. Fabrication of silica rod microcavity

A silica rod microcavity is fabricated with laser machining. A fused quartz rod is turned with an air spindle in a fabrication process using a lathe. The material surface is vaporized using $CO_2$ laser machining. There are two procedures when fabricating silica rod microcavities. First procedure is surface processing. This procedure is conducted to change the diameter of the fused quartz rod. The second procedure is laser cutting. After processing the surface, the resonator shape is fabricated by laser cutting. Figure 1 shows the silica rod microcavity fabrication procedure.

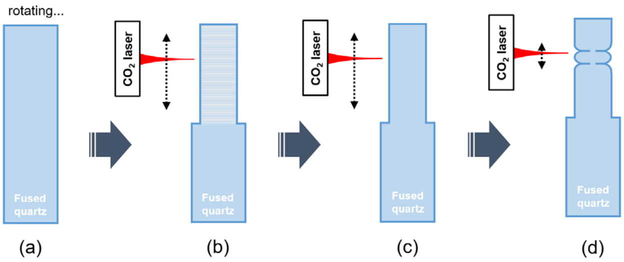


Fig. 1: Fabrication of silica rod microcavity. (a) Fused quartz rod turning with air spindle. (b) Surface processing using $CO_2$ laser machining. (c) Surface processing to anneal material surface. (d) $CO_2$ laser cutting to shape resonator.

## 4. Characterization of silica rod microcavity

We characterized the fabricated silica rod microcavity. The quality factor of the silica rod microcavity was about $10^8$. In the experiment, a tapered fiber a few micrometers in diameter was used to couple light to the microcavity. CW light from a tunable laser source was input into the microcavity and we measured the transmission spectrum. The quality factor of the microcavity was measured from the transmission spectrum. Figure 2 shows an image of the microcavities.

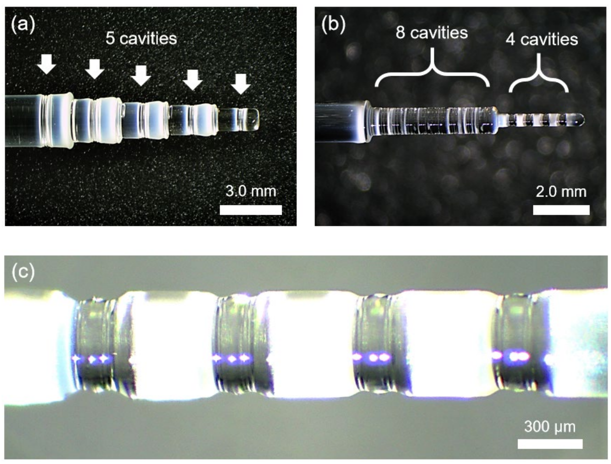


Fig. 2: Silica rod microcavities. (a) From the left, the microcavity diameters are 2.5, 2, 1.7, 1.4, and 1.1 mm. (b) Silica rod microcavities with 1-mm and 450-μm diameters. (c) Enlarged image of 450-μm silica rod microcavities in (b).

Figure 3 shows the transmission spectrum of a silica rod microcavity with a 1.3-mm diameter (FSR = 55.3 GHz). The quality factor is $10^8$.

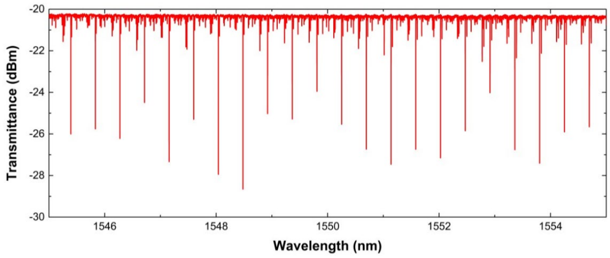


Fig. 3: Transmission spectrum of silica rod microcavity with 1.3-mm diameter.

We observed a third order nonlinear optical effect with a fabricated silica rod microcavity. Figure 4 shows the Kerr comb spectra generated via cascaded four-wave mixing in a silica rod microcavity. By sweeping the pump wavelength from the red side to the blue side, Kerr comb is generated in the microcavity. Figure 4 (a) shows a Kerr comb spectrum from a 450-µm silica rod microcavity (FSR = 145 GHz) and Fig. 4 (b) shows a Kerr comb spectrum from a 2.5-mm silica rod microcavity (FSR = 27.8 GHz).

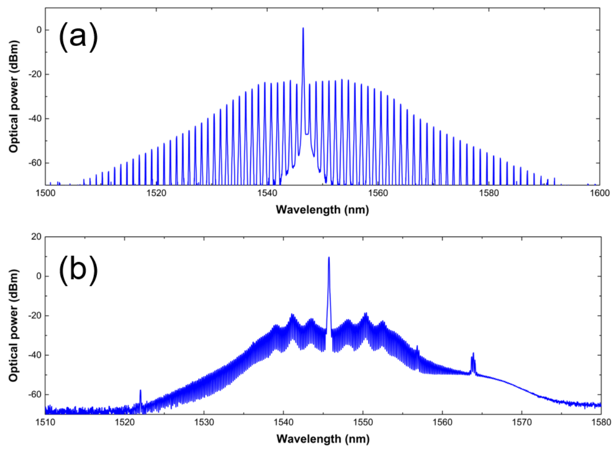


Fig. 4: Kerr comb spectra from silica rod microcavities. (a) Kerr comb from a silica rod microcavity 450 µm in diameter (FSR = 145 GHz), (b) Kerr comb from a silica rod microcavity 2.5 mm in diameter (FSR = 27.8 GHz)

In addition, a Raman comb realized by stimulated Raman scattering in a silica rod microcavity was also observed. Silica has a large and very broad Raman gain because of its amorphous structure. Figure 5 shows a Raman comb spectrum from a 450-µm silica rod microcavity. Figure 5 (a) shows the first Raman Stokes light, the second Raman Stokes light, and anti-Stokes light generated by stimulated Raman scattering. A Raman comb was generated from each frequency component. Figure 5 (b) shows a Raman comb generated by stimulated Raman scattering and a Kerr comb generated simultaneously by cascaded four-wave mixing. In this case, the Kerr comb generated around the pump wavelength and the Raman comb generated far from the pump wavelength were excited in the same mode family, and so the Kerr comb was spread broadly towards the red side by the Raman gain. When generating a broadband Kerr frequency comb, the group velocity dispersion of the microcavity is important. To control the group velocity dispersion of the microcavity, the material or the structure of the microcavity must be changed. The structure of a silica rod microcavity can be controlled by controlling the power of the $CO_2$ laser, and the exposure time during laser processing. We must investigate the fabrication method and improve it to control the shape of the microcavity. A silica rod microcavity has a larger mode volume and a larger radius of curvature than other microcavities such as a silica toroid microcavity, and so many high order cavity modes can be excited. To identify the cavity mode and excite the intended specific mode is difficult because of the characteristic of silica rod microcavities.

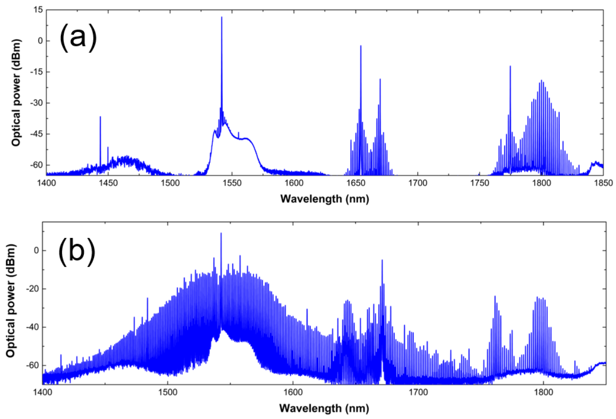


Fig. 5: Stimulated Raman scattering in a silica rod microcavity. (a) Raman comb spectrum from first order Raman Stokes light and second order Raman Stokes light. (b) Kerr comb spectrum with Raman comb. The Kerr comb was spread broadly towards the red side by Raman gain.

## 4. Conclusion

We fabricated silica rod microcavities. The quality factor of the microcavities is about $10^8$. Using the fabricated silica rod microcavity, we observed a third order nonlinear optical effect, such as a Kerr frequency comb by cascaded four-wave mixing, Raman comb by stimulated Raman scattering.

## References

[1] F.-L. Hong, OYOBUTSURI **36**(2), 60-67 (2007).
[2] P. Del'Haye, T. Herr, E. Gavartin, M. L. Gorodetsky, R. Holzwarth, and T. J. Kippenberg, Phys. Rev. Lett. **107**, 063901 (2011).
[3] T. J. Kippenberg, R. Holzwarth, and S. A. Diddams, Science **332**, 555-559 (2011).
[4] P. Del'Haye, S. A. Diddams, and S. B. Papp, Appl. Phys. Lett. **102**(22), 221,119 (2013).
[5] J. Pfeifle, V. Brasch, M. Lauermann, Y. Yu, D. Wegner, T. Herr, K. Hartinger, P. Schindler, J. Li, D. Hillerkuss, et al., Nat. Photon. **8**(5), 375–380 (2014).
[6] L. Maleki, Nat. Photon. **5**(12), 728 (2011).

# Dispersion compensation and phase control for Kerr combs

Takuma Nagano (M2)

When a CW laser is incident on a microscale whispering gallery mode (WGM) resonator, it is possible to generate equidistant longitudinal mode groups by using a nonlinear response called four wave mixing. Although this broadband spectrum is an optical Kerr comb, many problems remain as regards realizing stability equivalent to that of a frequency comb. We have developed a low threshold optical Kerr comb generation using a silica toroid resonator (and a silica rod resonator) and constructed and evaluated a stabilization system in that time domain. Also, with arbitrary phase control, we observed a repetitive increase in the integral multiple of the pulse.

**Key words:** Kerr comb, line-by-line waveform shaping, phase control

## 1. About the annual report

An optical Kerr comb is a light flux with a constant spectral interval generated from a micro optical resonator. When they are in a mode synchronous state, they are called optical Kerr frequency combs. However, when the carrier envelope offset (CEO) is not locked, it is distinguished from an optical frequency comb [1]. To generate an optical frequency comb, it is necessary to inject a high-power laser into a long-distance nonlinear fiber, and this was impossible without a very large device. On the other hand, in a micro optical resonator, with high optical confinement and thanks to the property of silica, which is amorphous, the third order nonlinear optical effect (optical Kerr effect) is induced, and an optical Kerr comb can be generated. It would be easy to imagine that various applications could be realized if it were possible to generate an optical Kerr frequency comb with low power from an inexpensive and integratable element such as a silica toroid resonator. However, it is not easy to apply mode locking to an optical Kerr comb, and various efforts have been made in experiments using each type of micro optical resonator [2].

## 2. Pulse shaper

Since picosecond pulse compression was reported in the latter half of the 1960s [3], a waveform shaping technique with coherent control has been developed for femtosecond pulsed lasers . Femtosecond pulsed lasers are not easy to control directly in the time domain because of their ultrafast properties. Among the control techniques, the most widely used is the frequency synthesizer method. By using two pairs of diffraction gratings and lenses and employing filtering in the frequency domain, modulation is applied to the optical pulses, so that an element exhibiting a high-speed response is not required. On the frequency side, to modulate both amplitude and phase, a mask is employed called a spatial light modulator (SLM) based on a space address. This setup, which was proposed by C. Froehly et al., is a prototype for shaping a 30 ps input pulse [4].

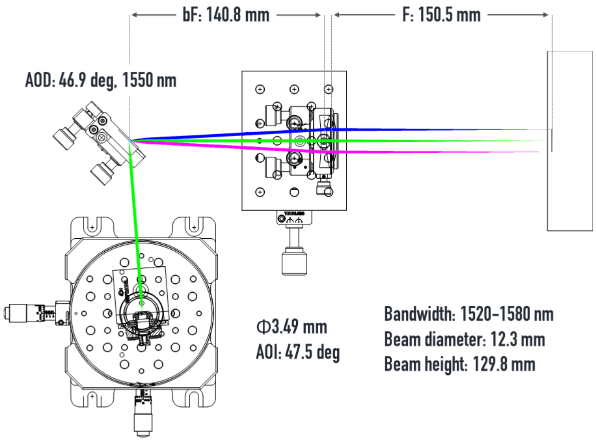


Fig. 1-1: Design drawing of waveform shaper

We first constructed a waveform shaper to enable us to apply dispersion compensation to each of the optical Kerr spectra generated using a silica toroid resonator with a diameter of 100 μm. The methods are described below.

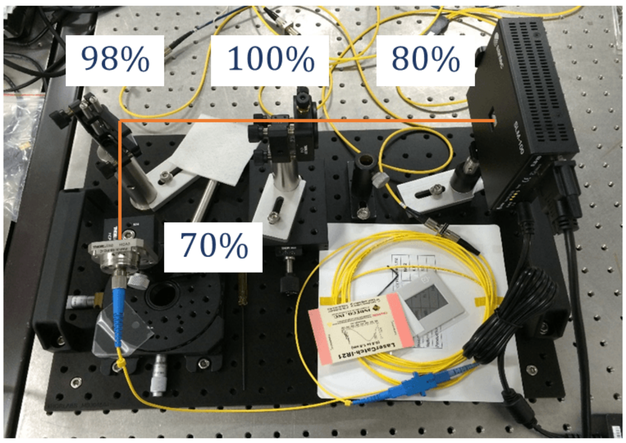


Fig. 1-2: Pictures actually constructed

First, a reflective liquid crystal on silicon (LCOS) -

SLM [5] was used for alignment simplification. Because 4f becomes 2*f* (*f* is the focal length of the lens) the influence of dispersion caused by misalignment (deviation from the ideal state) [6] can be greatly diminished or made negligible in that a symmetrical optical path can be achieved naturally.

Second, a transmission type diffraction grating was used to realize a high diffraction efficiency over a wide band [7].

The theoretical transmittance value was -2.7 dB, and the measured value was -3.2 dB. By using this value, each spectrum of the optical Kerr comb is provided with phase modulation [8].

### 3. Dispersion compensation

An optical Kerr spectrum was obtained from the silica toroid micro optical resonator with a diameter of 200 μm, as shown in Fig. 2-1. An arbitrary phase modulation was given to each of these spectra, and dispersion compensation was applied so as to obtain a Fourier limit pulse. The control program was created by processing. The autocorrelation waveform obtained at this time is shown in Fig. 2-2.

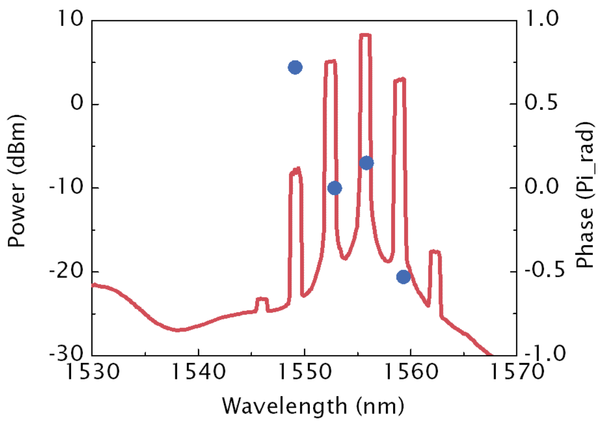


Fig. 2-1: Figure 2-1: Spectrum (red) and phase modulation (blue) of an optical Kerr comb generated using a silica toroid micro optical resonator with a diameter of 200 μm.

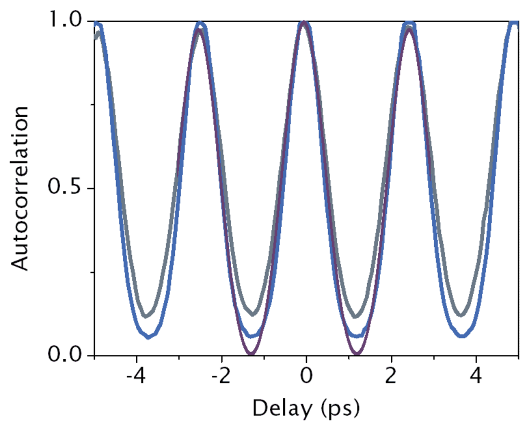


Fig. 2-2: Comparison of autocorrelation waveform before dispersion compensation (gray) (blue) with calculation (purple)

Here, the repetition frequency of the Kerr comb was 0.37 THz, the correlation width was 1.06 ps, and the pulse width was 0.69 ps.

### 4. Phase control

Experiments were conducted to apply a further phase control to the Fourier limit pulse obtained as described in 3 and to aim for a repetitive increase by employing an integral multiple. This was accomplished using a silica rod resonator 400 μm in diameter.

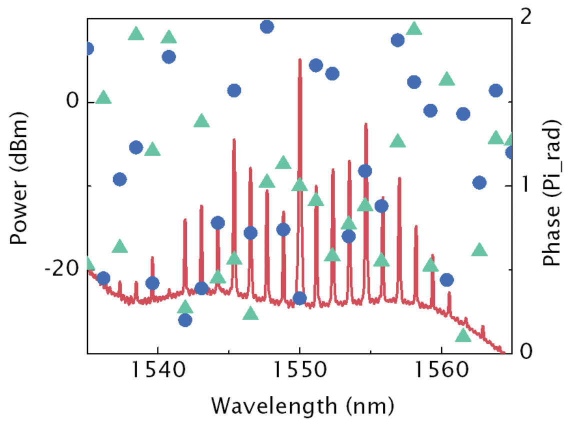


Fig. 3-1: Spectrum (red) and dispersion compensation (blue) and phase modulation amount (green) of an optical Kerr comb generated using a silica rod resonator with a diameter of 400 μm.

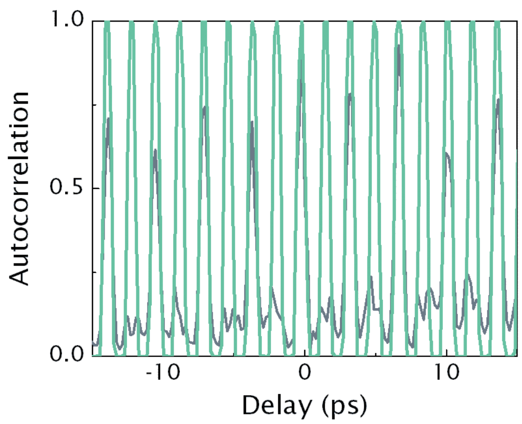


Fig. 3-2: Autocorrelation waveform before modulation (gray) (green)

At this time, the correlation width was 1.37 ps, and the pulse width was 0.89 ps.

### 5. Summary

A high precision femtosecond pulsed laser waveform shaper operating in the communication wavelength band was constructed. The phase modulation was designed to be added to each of the optical Kerr comb spectra generated by the micro optical resonator, and an optical setup for high transmittance and zero dispersion was constructed. As regards the dispersion compensation, an interactive interface was created and employed as an SLM mask so that the phase of the optical Kerr could be manipulated visually and intuitively. As a result, a high repetition rate of 0.37 THz and a high contrast Fourier limit pulse were obtained. By adding further phase modulation, the above-mentioned twice repeating optical pulse train was observed. This is the first observation of an iterative increase in an integral multiple by line-by-line phase control (by means other than the use of dispersion compensation fiber). In addition, the same experiment was carried out using a silica rod resonator with a diameter of 400 μm in order to perform the above dispersion compensation and phase control for more (optical Kerr) modes. At this time, we introduce a mask program that can newly manipulate up to 5th order dispersion, and simultaneously control more than 20 longitudinal modes.

## References

[1] T. Kippenberg, R. Holzwarth and S. Diddams, Science 332 **555** (2012).
[2] P. Del'Haye, O. Arcizet, A. Schliesser, R. Holzwarth and T. J. Kippenberg, Phys. Rev. Lett. **101** 053903 (2008).
[3] R. A. Fisher and J. A. Fleck, Appl. Phys. Lett. 1**5** 287 (1969).
[4] C. Froehly, B. Colombeau and M. Vampouille, Progress in Optics **20** 63 (1983).
[5] K. Bauchert, S. Serati and A. Furman, Advances in liquid crystal spatial light modulators, Proc. SPIE **4734**, Optical Pattern Recognition XIII, (6 March 2002).
[6] T. Tanabe, H. Tanabe, Y. Teramura and F. Kannari, J. Opt. Soc. Am. B **19** 2795 (2002).
[7] H. T. Nguyen, B. W. Shore, S. J. Bryan, J. A. Britten, R. D. Boyd and M. D. Perry, Opt. Lett. **22** 142 (1997).
[8] A. Weiner, Opt. Comm. **284** 3669 (2011).

# Accurate numerical modeling of a coupled cavity system and dark soliton generation

Yusuke Okabe (M2), Takumi Kato (D2), Shun Fujii (M1), Ryo Suzuki (D1)

A Kerr comb is expected to be a new optical frequency comb laser. To broaden the spectra for carrier-envelope offset control, a new dispersion control method using another cavity has been proposed and demonstrated experimentally. The experimental results revealed a new bandwidth Kerr comb, however, the theoretical study used an approximated model that did not take the second cavity into consideration. We describe the modeling of a 2-cavity system and perform a numerical simulation of dark soliton generation in a normal dispersion regime.

**Keyword**：Optical frequency comb; Microcavity device; Coupled resonators; Dark soliton

## 1. Background

A Kerr comb is created by generating a cascade of other spectra with a 3rd order nonlinear optical effect in a high-$Q$ microcavity in an anomalous dispersion regime [1]. It can be made more cheaply, more compact, and with a higher repetition rate than an optical frequency comb (OFC). This means that smaller devices may be realized by replacing the OFC with a Kerr comb. However, because a microcavity has a narrow anomalous dispersion regime, we cannot obtain a Kerr comb that is mode-locked and that spans one octave [2].

Recently, to overcome this problem, research has been under way on Kerr comb generation in several normal dispersion regimes, where phase-matching cannot be satisfied [3][4]. Here, the principle is that mode-splitting induced by coupling two cavities can control the dispersion and so four-wave mixing can be realized because phase-matching is obtained. An experimental mode-locked Kerr comb produced by the above method has been reported [4] but the theoretical research used an approximated model of a one cavity system. In this research, we constructed an accurate model of a coupled cavity system by using coupled mode theory (CMT) and simulated mode-locked Kerr comb generation in a normal dispersion regime.

## 2. Coupled cavities

Coupled cavities are two cavities that are sufficiently close together (Fig. 1). When light is input into cavity A, some of the light moves to cavity B. Kerr comb generation is realized using this system because a Kerr comb occurs in cavity A and dispersion is controlled by cavity B. The merit of this 2-cavity system is that it offers arbitrary dispersion control by changing the size or material of cavity B.

When two cavities are coupled, the same resonant frequency will be split into two resonant frequencies (Fig. 2). This phenomenon is called mode-splitting; it changes the effective free spectral range (FSR) at the frequency so that the effective dispersion can be regarded as different from the original. Kerr comb generation requires that phase-matching be satisfied, and this can only be realized in an anomalous dispersion regime. However, the dispersion control method enables phase-matching in even a normal dispersion regime [3][4].

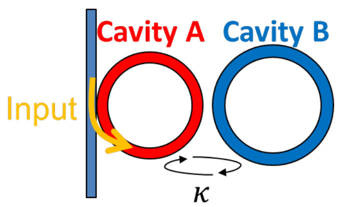


Fig. 1. Schematic model of coupled cavities. A light (yellow) input into cavity A (main cavity; red) and cavity B (auxiliary cavity; blue) controls the dispersion of cavity A. $\kappa$ is the coupling strength.

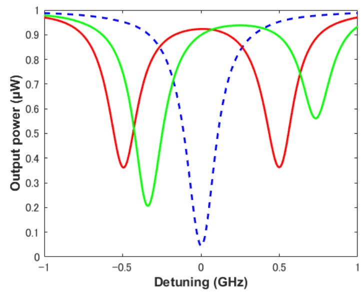


Fig. 2. Schematic graph of mode-splitting. It shows the detuning from the original resonant frequency. The blue dotted line shows the original resonant frequency. When two resonant frequencies correspond perfectly, it splits the same two resonant frequencies (red). If the original resonant frequencies are slightly different, the split frequencies move and change the resonant dip.

## 3. Kerr comb generation using coupled cavity system

There has been no accurate model of a coupled cavity system until now and so we constructed a model using CMT (Eq. 1). CMT can describe coupled cavities because it has equations for each resonant frequency; a nonlinear Schrödinger equation cannot describe it. Where $\mu$, $\theta$ are the mode numbers (mode number 0 means the center resonant frequency nearest the input), A, B are the mode amplitudes of each cavity, $\gamma$ is the loss ($\gamma = \gamma_{\rm ext} + \gamma_{\rm int}$), $\delta$ is the Kronecker delta, $\omega_\mu$ is the resonant frequency, $\omega_{\rm in}$ is

$$\begin{aligned}
\frac{\partial A_\mu}{\partial t} &= -\frac{\gamma_{A\mu}}{2}A_\mu + \delta_\mu\sqrt{\gamma_{Aext}}A_{in}e^{i(\omega_{Ain}-\omega_{Ao})t} + ig_A\sum_{\alpha,\beta,\gamma}A_\alpha A_\beta^* A_\gamma e^{i(\omega_{A\alpha}-\omega_{A\beta}+\omega_{A\gamma}-\omega_{A\mu})t} + i\delta_{\omega A_\mu-\omega B_\theta}\frac{\kappa_\theta}{2}B_\theta \\
\frac{\partial B_\mu}{\partial t} &= -\frac{\gamma_{B\mu}}{2}B_\mu + \delta_\mu\sqrt{\gamma_{Bext}}B_{in}e^{i(\omega_{Bin}-\omega_{Bo})t} + ig_B\sum_{\alpha,\beta,\gamma}B_\alpha B_\beta^* B_\gamma e^{i(\omega_{B\alpha}-\omega_{B\beta}+\omega_{B\gamma}-\omega_{B\mu})t} + i\delta_{\omega B_\mu-\omega A_\theta}\frac{\kappa_\theta}{2}A_\theta
\end{aligned} \tag{1}$$

the input light frequency, $g$ is the nonlinear coefficient, and $\kappa$ is the coupling strength between the two cavities.

It takes a long time to simulate these equations because they consist of several hundred differential equations. To avoid this, this simulation was performed using a fast Fourier transformation [6].

## 4. Kerr comb simulation

We simulated Kerr comb generation by the method described in Section 3. We used parameters from Ref. [4]. The Kerr comb was generated in a normal dispersion regime. Note that we assumed that the coupling strength was 800 MHz and that the resonant frequency and the FSR of the auxiliary cavity were 220 MHz higher, and 200 MHz smaller than those of the main cavity, respectively.

We show the simulation results in Fig. 3.

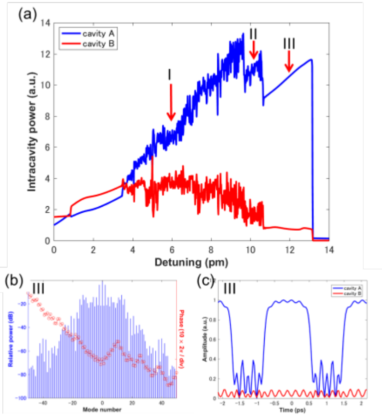


Fig. 3. Kerr comb simulation. (a) Intracavity power vs. detuning from mode 0. The blue and red lines show the intracavity powers of cavities A and B, respectively. **I**. Chaotic state. **II**. Stable but noisy. **III**. Mode-locked. (b) Optical spectrum of cavity A at **III**. The blue bar and red circles show the mode amplitudes and the phase, respectively. (c) The time waveforms of cavity A (blue) and cavity B (red) at **III**. The mode-locked time waveform is called a dark soliton.

In this simulation, we swept the input frequency from a higher frequency to a lower frequency. Figure 3(a) shows the intracavity power for detuning from the center frequency; **I** is the chaotic state, **II** is the static state but it had noise, **III** is the mode-locked state. The blue and red lines show the intracavity powers of cavities A and B, respectively. Figure 3(b) shows the optical spectrum of cavity A at **III**. The blue bar and red circles show the mode amplitudes and the phase, respectively. Note that when the Kerr comb is mode-locked in a normal dispersion regime, the phase becomes V-like or a slope. The soliton position determines the phase shape. Figure 3(c) shows the time waveforms of cavity A (blue) and cavity B (red) at **III**. The soliton is valley-shaped compared with a usual pulse, which looks like a delta function, and so the soliton is called a dark soliton (and the usual soliton is called bright soliton.) Since a dark soliton usually occurs in a normal dispersion regime (the bright soliton usually in an anomalous dispersion regime) and the shape was the same as in previous research (Ref. [4]), our model accurately describes the dynamics of Kerr comb generation with coupled cavities.

Note that there are two points arise from the experimental results in the previous research (Ref. [4]). One is that the chaotic state **II** did not exist and the other is that the a stable state did not move to another stable state (state **II** to state **III**) in the experiment. We expect this behavior to provide new perceptions regarding the Kerr comb.

## 5. Conclusion

We constructed an accurate model of a coupled cavity system using CMT. We then simulated Kerr comb generation in the model with an FFT. As the result, we obtained a mode-locked Kerr comb, and a dark soliton, that matched previous experimental results. However, there are two different points. They are the presence or absence of a chaotic state and of a stable state moving to another stable state. If we reveal these dynamics, we could gain a new perception of the Kerr comb.

## Reference

[1] P. DelHaye, A. Schliesser, O. Arcizet, T. Wilken, R. Holzwarth, and T. Kippenberg, "Optical frequency comb generation from a monolithic microresonator," Nature **450**, 1214-1217 (2007).

[2] P. DelHaye, T. Herr, E. Gavartin, M. Gorodetsky, R. Holzwarth, and T. Kippenberg, "Octave spanning tunable frequency comb from a microresonator," Phys. Rev. Lett. **107**, 063901 (2011).

[3] C. Godey, I. Balakireva, A. Coillet, and Y. Chembo, "Stability analysis of the spatiotemporal Lugiato-Lefever model for Kerr optical frequency combs in the anomalous and normal dispersion regimes," Phys. Rev. A **89**, 063814 (2014).

[4] X. Xue, Y. Xuan, Y. Liu, P. Wang, S. Chen, J. Wang, D. Leaird, M. Qi, and A. Weiner, "Mode-locked dark pulse Kerr combs in normal-dispersion microresonators," Nat. Photon. **9**, 594-600 (2015).

[5] H. Haus, "Waves and fields in optoelectronics," (Prentice-Hall 1984).

[6] T. Hansson, D. Modotto, and S. Wabnitz, "On the numerical simulation of Kerr frequency combs using coupled mode equations," Opt. Commun. **312**, 134-136(2014).

# Fabrication of Crystalline Microresonator by Hand Polishing

Mika Fuchida (B4)

A crystalline microresonator is a whispering gallery mode (WGM) microresonator that is attractive for generating a stable optical Kerr comb because of its highly efficient confinement of light. In this research, we fabricated an ultra-high Q crystalline microresonator by hand polishing.

**Key Words**：Microresonator, Fabrication of Crystals

## 1. Background

The performance of microresonators can be defined in terms of quality factor, which represents how long light can be confined inside a cavity. Elements that comprise the quality factor related to the amount of loss, such as the absorption loss of the material, the scattering loss on the surface of the resonator, the radiation loss due to the evanescent field of the WGM propagation, and the coupling loss induced by the coupling between the resonator and the waveguide. The threshold power when generating an optical Kerr comb inside a microresonator can be expressed as

$$P_{th} \propto V/Q^2$$

where V is the mode volume [2]. Therefore, to generate Kerr combs with less input power, a microresonator with an ultra-high Q is desired.

Ultra-high Q microresonators are generally fabricated by hand polishing [1]. While spinning the resonator on a spindle, a diamond knife is applied to the rim of the resonator to obtain a round shape. The resonator is then polished using diamond polishing paste. A quality factor of $Q = (6.3 \pm 0.8) \times 10^{10}$ is obtained using this method.

In this research, we used calcium fluoride, which is known for its high Q factor in absorption, and we employed hand polishing at the rim to avoid scattering loss and to increase the quality factor.

## 2. Fabrication of a crystalline microresonator

The process of fabricating a crystalline microresonator can be divided into 3 steps. Figure 1 is a flow chart of the fabrication process. First, a calcium fluoride wafer is cut to approximately the same size as the intended diameter of the resonator. Next, the rim of the resonator is shaped with a knife or a polishing paper. Finally, the resonator is polished to obtain a smooth surface.

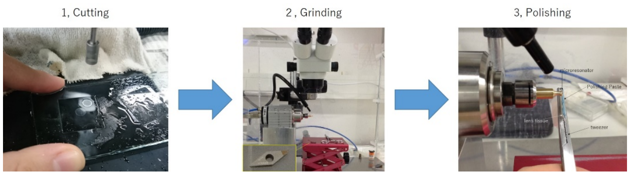


Fig. 1 : Flow chart of crystalline microresonator fabrication process .

## 3. Cutting out the resonator

Cutting out the resonator is illustrated in Fig. 2(a). A calcium fluoride wafer is affixed to an aluminum or glass plate, using an adhesive wax. Then, a diamond core drill is secured to a small drilling machine. The diamond core drill is cylindrical but hollow, and so a disk can be cut from the wafer. By lowering the core drill vertically and gently, the resonator can be cut out without huge cracks. A cut out resonator is shown in Fig. 2(b), where the wax is well cleaned with no serious damage.

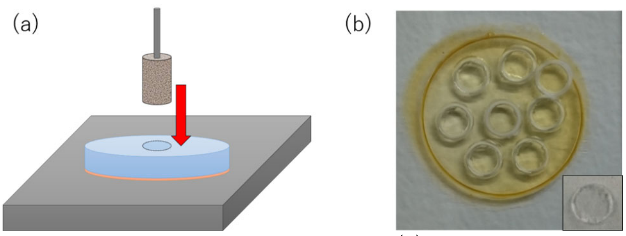


Fig. 2 : Cutting out the $CaF_2$ Wafer. (a) Illustration of the cutting out process (b) Cut out resonator

## 4. Grinding the resonator (rough polishing)

A cut out resonator is affixed to a metal post as shown in Fig. 3(a). The metal post is secured to an air bearing spindle, and the rim is ground using a knife as shown in the inset in Fig. 1, or a polishing paper. When shaping the rim, it is important that the propagation point extends further, opposite where the metal lies, and a knife or polishing paper is applied cautiously to ensure that no excessive force is applied to the resonator, which could cause cracks or damage. A microscope is used to obtain an overhead view and thus clearly determine how the resonator is being ground. The view is shown in Fig. 3(b). The knife is applied from the side nearest the user, and the polishing paper is applied from the opposite side.

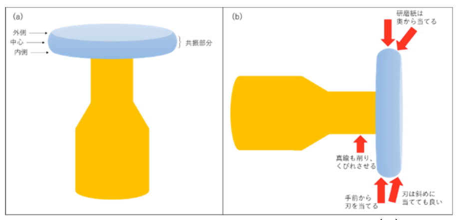


Fig. 3 : Grinding the $CaF_2$ resonator. (a) Metal post

(yellow) and resonator (blue). (b) Red arrows indicate how the tools are applied.

## 5. Polishing the resonator

The resonator is polished with the same apparatus used when grinding as shown in Fig. 4(a). A sufficient amount of polishing paste is used on a lens tissue held with tweezers, while adding a sufficient amount of pure water. Polishing paste with grain sizes of 3 $\mu m$, 1 $\mu m$, 0.25 $\mu m$, and 0.05 $\mu m$ is used in this order, and the resonator surface is carefully polished with grains touching, and tissue not touching. Polishing is continued until there are absolutely no cracks, including spot like cracks, as shown in Fig. 4(b).

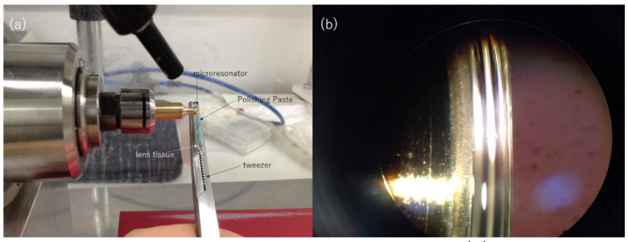


Fig. 4 : Polishing the $CaF_2$ resonator. (a) Setup and apparatus used for grinding and polishing. (b) Resonator after hand polishing

## 6. Measurement of $Q$ Factors

To check that a microresonator with an ultra-high Q factor was fabricated, we measured the Q factor of the $CaF_2$ resonator. The experimental setup and the resonator we inspected are shown in Fig. 5. The diameter of the resonator is approximately 3.6 mm. We used a Mach-Zehnder interferometer with a resonance of 1 GHz to obtain the exact frequency of the frequency swept laser.

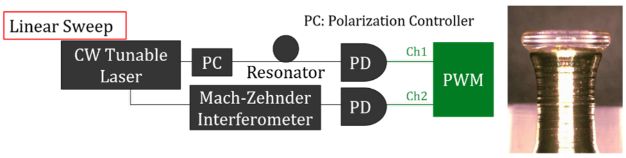


Fig. 5 : Experimental setup for the $Q$ Factor measurement.

The obtained transmission spectrum is shown in Fig. 6(a). The Q factor calculated by measuring the HWHM linewidth of the deepest dip was $Q = 2.2 \times 10^9$. The linewidth of the dip was about 100 kHz, the same as that of the tunable laser, so the obtained Q factor was the maximum that can be measured with the setup used in this experiment.

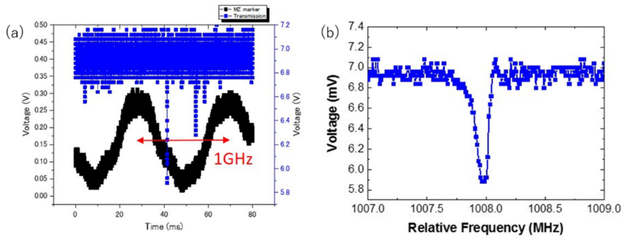


Fig. 6 : Transmission spectrum of the fabricated resonator.

## 7. Conclusion

A WGM microresonator was fabricated from a $CaF_2$ wafer, using a hand polishing method. The fabricated device had an ultra-high quality factor of $Q = 2.2 \times 10^9$.

## References

[1] T. J. Kippenberg, R. Holzwarth, and S. A. Diddams, Science **332**, 555-559 (2011).
[2] Ivan S. Grudinin, Vladimir S. Ilchenko, and Lute Maleki, Phys. Rev. A 74, 063806 (2006).

## Acknowledgements

I would like to thank Mr. R. Wolf and Dr. I. Breunig of Freiburg University, for providing the apparatus and teaching me the method that I used for grinding and polishing the resonator.

# Highly accurate dispersion measurement of an optical microcavity

Hiroki Itobe (M2) Mika Fuchida (B4)

To put an optical Kerr comb generated in an optical microcavity into practical use, the microcavity must exhibit an anomalous dispersion over a band of one octave. In this research, we fabricated a microcavity with anomalous dispersion over a wide band by tailoring the cross sectional shape of the microcavity and manipulating the dispersion. Furthermore, to measure the dispersion of the fabricated microcavity with high accuracy, we developed a dispersion measurement method using an optical frequency comb.

**Key words:** Optical microcavity; Dispersion; Optical Kerr comb; Optical Frequency comb

## 1. Introduction

An optical microcavity is also called a "container that confines light", and can enhance the interaction between light and a given material by trapping light inside it. It is known that the intensity of the interaction between light and a given material is proportional to the square of $Q$, which is the light trapping efficiency of the microcavity, and inversely proportional to $V$, which is the volume of the microcavity. In particular, a microcavity made of calcium fluoride ($CaF_2$), which has a small light absorption coefficient, has both an extremely high $Q$ and a very small $V$ that can be realized thanks to the recent development of cutting technology.

## 2. Bandwidth of optical Kerr comb and dispersion of microcavity

An optical Kerr comb is a phenomenon observed by trapping light in a microcavity. Light is generated at a constant frequency interval in the frequency domain and is similar to an optical frequency comb, which is a phenomenon generated by using a mode locked laser. A microcavity is cheaper and smaller than a mode locked laser. However, to determine the absolute frequency of an optical Kerr comb, the maximum frequency must be at least twice the minimum frequency, in other words, the optical Kerr comb must have a band of 1 octave or more. Furthermore, to generate an optical Kerr comb, the microcavity must have an anomalous dispersion. In other words, the effective refractive index of the microcavity decreases as the frequency of the light increases. Considering the above, it can be said that a microcavity for use as a practical optical Kerr comb source is one with an anomalous dispersion of 1 octave or more. The dispersion of the microcavity is expressed by the sum of the structural dispersion derived from the cross-sectional shape of the microcavity and the material dispersion derived from the effective refractive index of the microcavity material. In this study, by manipulating the structural dispersion by tailoring the cross-sectional shape of the microcavity using a cutting process [1] and adopting $CaF_2$ with a material dispersion close to 0 in the telecommunication wavelength band as the microcavity material, we designed, fabricated, and evaluated a microcavity with an anomalous dispersion of 1 octave or more, which we hereafter refer to as a "dispersion managed microcavity".

## 3. Design of dispersion managed microcavity

The dispersion managed microcavity is manufactured by cutting a $CaF_2$ rod, and so it has the shape shown in Fig.1 (a). The cross-sectional shape to be designed is a region where light is trapped and which is shown in Fig.1 (b). The simulation was carried out by setting the parameters $a$, $b$, $c$, and $r$. As a result, by adopting a structure where $a$ = 5 μm, $b$ = 6 μm, $c$ = 5 °, and $r$ = 262 μm, the electromagnetic field distribution shown in Fig. 2 (a) was obtained along with an anomalous dispersion at a bandwidth of 1.12 octaves in the 1313-2771 nm range.

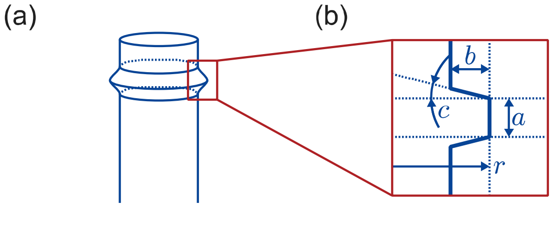


Fig.1: Structure of dispersion managed microcavity.

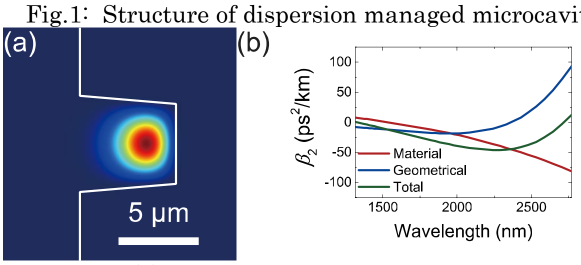


Fig.2: (a) Electromagnetic field distribution of dispersion managed microcavity.
(b) Dispersion of dispersion managed microcavity.

## 4. Fabrication of dispersion managed microcavity

The dispersion managed microcavity was fabricated by using the ultra-precision nano processing machine shown in Fig.3 and located at Kakinuma Laboratory, Department of System Design Engineering, Faculty of Science and Technology, Keio University. Figure 4 shows the fabricated dispersion managed microcavity. The result of a $Q$ value measurement is shown in Fig. 5, and $Q = 1.2 \times 10^6$ μm was obtained.

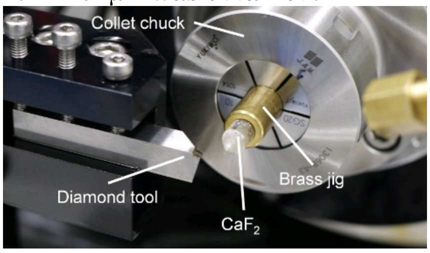


Fig.3: Fabrication of dispersion managed microcavity.

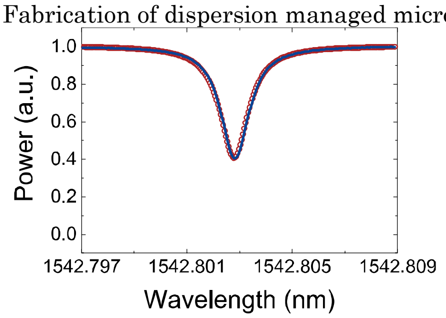


Fig.4: Result of $Q$ value measurement of dispersion managed microcavity.

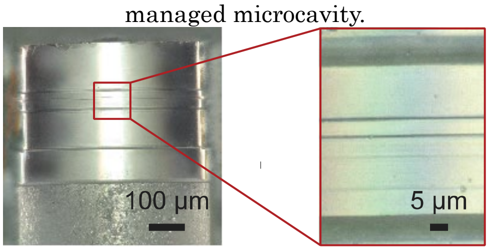


Fig.5 Fabricated dispersion managed microcavity.

## 5. Evaluation of dispersion managed microcavity

The dispersion of the dispersion managed microcavity was calculated as follows by using the transmittance spectrum shown in Fig. 6.

$$\beta_2 = -\frac{1}{4\pi^2 r} \cdot \frac{\Delta\mathrm{FSR}}{\mathrm{FSR}^3} \tag{1}$$

$$\mathrm{FSR} = \frac{\nu_{l+m} - \nu_{l-m}}{2m} \tag{2}$$

$$\Delta\mathrm{FSR} = \frac{\nu_{l+m} - 2\nu_l + \nu_{l-m}}{m^2} \tag{3}$$

Because FSR is the difference between the resonant frequencies and ΔFSR is the difference between the resonant frequencies, it can be said that a high accuracy is required for the resonant frequency. In this research, we developed a highly accurate dispersion measurement method by using an optical frequency comb, which has already been employed as high precision frequency reference. Figure 7 shows how to obtain the frequency reference [2].

1. When lights with frequencies $f_1$ and $f_2$ are combined, a beat signal whose frequency is $|f_1 - f_2|$ is generated via difference frequency mixing. When the optical frequency comb and the light of a tunable laser diode are combined, the beat signal whose frequency changes periodically in the $0 < f_{\mathrm{Beat}} < f_r$ range, where $f_r$ is the repetition frequency of the optical frequency comb.
2. The beat signal is expressed as a triangular wave when time ($t$) is expressed by the horizontal axis and frequency ($f$) by the vertical axis. This signal is passed through a band pass filter, and a signal extracted in a specific frequency band is called the beat criterion.
3. The beat criterion is expressed as a periodic signal for each of the even-numbered and odd-numbered peaks when time ($t$) is expressed by the horizontal axis and voltage ($V$) by the vertical axis. The time at which the peaks is taken is called the frequency criterion.
4. Even-numbered and odd-numbered frequency criteria appear every time the frequency of the tunable laser diode changes by an amount corresponding to $f_r$. Therefore, the frequencies of the even-numbered and odd-numbered frequency criteria, $f_{\mathrm{even}}$ and $f_{\mathrm{odd}}$, are calculated as follows. $\Delta f$ is the frequency difference between the first and second frequency criteria and depends on the center frequency of the band pass filter ($f_{\mathrm{BPF}}$). $n$ is an integer of 0 or more.

$$f_{\mathrm{even}} = f_0 + nf_r \tag{4}$$

$$f_{\mathrm{odd}} = \Delta f + f_0 + nf_r \tag{5}$$

Figure 8 shows the dispersion calculated based on the method shown in Fig. 7. Because the measurement accuracy of the dispersion is insufficient, it will be necessary to reconsider the experimental setup and the calculation algorithm to realize a dispersion measurement with higher precision.

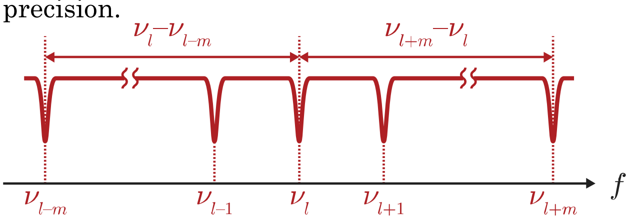


Fig.6: Transmittance spectrum.

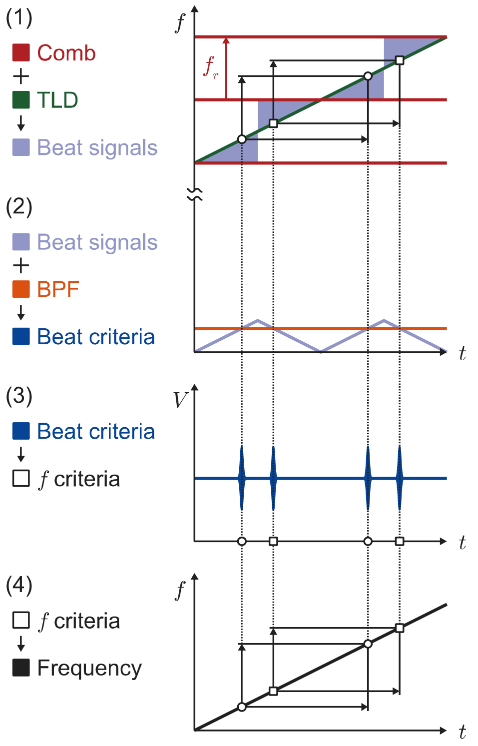


Fig.7: How to obtain frequency criteria.

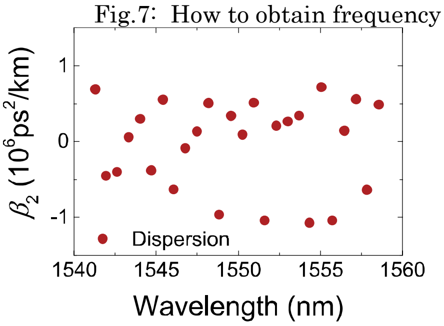


Fig.8: Calculated dispersion.

## 6. Conclusion

The results of the design, fabrication, and evaluation of the dispersion managed microcavity in this research are as follows. As regards the design, the calculated anomalous dispersion was 1.12 octaves. A dispersion managed microcavity with $Q$ = 1.2 × $10^6$ μm was fabricated. In the evaluation step, a highly accurate dispersion measurement was performed using an optical frequency comb.

## References

[1] I. S. Grudinin, and N. Yu, "Dispersion engineering of crystalline resonators via microstructuring," Optica **2**, 221 (2015).
[2] P. Del'Haye, O. Arcizet, M. L. Gorodetsky, R. Holzwarth, and T. J. Kippenberg, "Frequency comb assisted diode laser spectroscopy for measurement of microcavity dispersion," Nature Photonics **3**, 529 (2009).
[3] T. Herr, V. Brasch, J. D. Jost, I. Mirgorodskiy, G. Lihachev, M. L. Gorodetsky, and T. J. Kippenberg, "Mode spectrum and temporal soliton formation in optical microresonators," Phys. Rev. Lett. **113**, 123901 (2014).

# Photonic Crystal Demultiplexers Fabricated with Photolithography

Yuta Ooka (M2), Tomohiro Tetsumoto (D2), Nurul Ashikin Binti Daud (D3)

We demonstrate ultrasmall demultiplexers based on photolithographic photonic crystals. The footprint of the demultiplexers is 110 μm$^2$ per channel. Our in-plane demultiplexers are clad with silica, which makes them stable and easy to integrate with other silicon photonic devices. We describe two types of demultiplexers with spacings of 136 and 267 GHz. Integrated titanium nitride heaters allow us to precisely control the channel wavelength. We report a 2.5 Gbps transmittance experiment with sufficiently small crosstalk and discuss ways of achieving even lower crosstalk between channels.

**Keywords:** Photonic crystal, Silicon photonics, CMOS process, Photonic crystal demultiplexer, 2D-FDTD

## 1. Background

Demultiplexers (DeMUXs) have been developed in the field of silica arrayed waveguide gratings (AWGs). Silica AWGs have been developing and these are used in many commercial products, but they are approaching the fabrication size limit. It is difficult to increase the capacity of data transmittance with silica AWGs, although the increase in data traffic appears to be never ending. One of the devices being studied in relation to this problem is the silicon AWG [1]. This is better both in terms of compatibility with other silicon photonic devices, and as regards size due to its higher refractive index. There is another candidate for replacing conventional silica AWGs, namely silicon photonic crystal (PhC) DeMUXs. The main advantage is that PhC DeMUXs have a much smaller footprint. Thanks to its periodic structure, a silicon PhC confines light more tightly in a small area than bulk silicon does.

There have been some studies of silicon PhC DeMUXs, but problems remain when applicability is considered. A DeMUX with a 32 channel-100 GHz spacing capacity has been realized, and its footprint is 4050 μm$^2$, which corresponds to 100 μm$^2$ per channel [2]. However, when we consider the entire system in which this DeMUX is used in practice, , the direction of the demultiplexed lights is out of the PhC slab and the system needs additional bulky optics. Although in-plane type DeMUXs have been demonstrated, they have few channels and a large spacing [3]. Thus, it is necessary to realize an in-plane driven PhC DeMUX with a high capacity. There are other aspects that also need to be improved. In the previous studies the PhCs were fabricated with EB lithography and with a silica cladding, which relates to our target. The PhC DeMUXs proposed in this study solve the problems and have great potential for practical applications.

This report is about the work we undertook in fiscal 2016 in order to solve the above problem. Eight- and 16-channel DeMUXs are demonstrated with spacings of 267 and 136 GHz.

## 2. Design and working functions

Figure 1 (a) is a schematic of our proposed eight-channel DeMUX. The PhCs and input/output nanowires are 210 nm thick silicon slabs clad with silica. The DeMUX consists of eight width-modulated (WM) line defect type PhC nanocavities. We employed this type of nanocavity because this WM type is compatible with photolithography [4]. Signals couple to nanocavities with resonant wavelengths corresponding to the carrier wavelengths of the signals, and are dropped to output waveguides. To tune the resonant wavelengths of the nanocavities, the PhC has different lattice constant $a$ on the $x$-axis. Although Fig. 1(a) shows only an eight-channel PhC DeMUX, a 16-channel device was also fabricated.

Figure 1(a) is a SEM image, which was taken after the silica cladding of the DeMUX was removed with hydrofluoric acid.

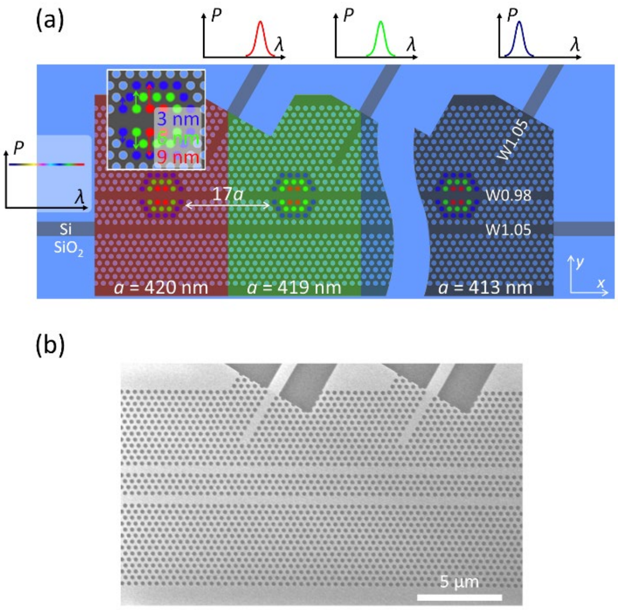


Fig. 1. (a) Schematic illustration of an eight-channel DeMUX. WM nanocavities are created by shifting the PhC hole positions 9, 6, and 3 nm. An eight-channel DeMUX has a step lattice constants of 1 nm. (b) SEM image of a fabricated DeMUX. The silica cladding was removed for the SEM observation.

## 3. Results

The transmission spectra of eight-channel DeMUXs are shown in the lower part of Fig. 2. This shows the DeMUX has a channel spacing of 267 GHz. The figure shows that clear DeMUX operation is possible. The upper figure is the result of tuning. It can be seen that linear tuning is successfully realized, and that the range of this tuning is larger than the channel spacing.

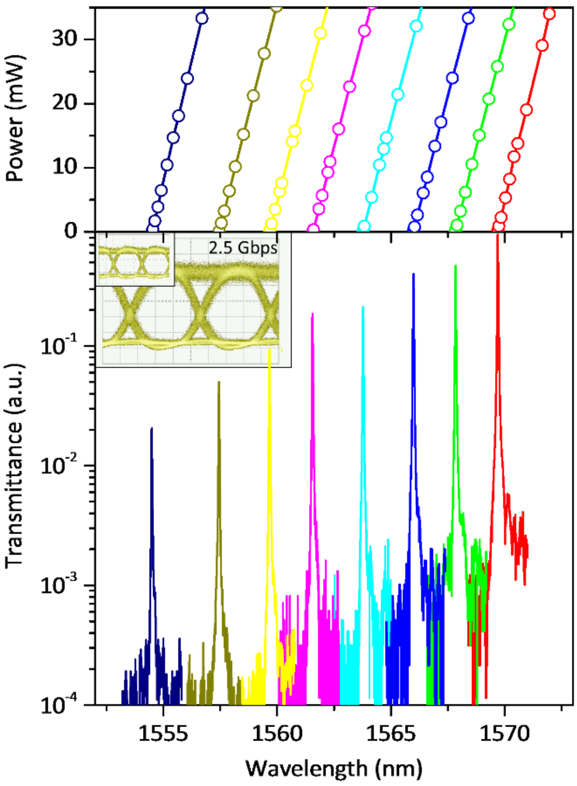


Fig. 2. Top: heater tunability of the eight-channel DeMUX. Bottom: transmission spectrum of an eight-channel DeMUX. Insets: eye diagrams of the output at the red channel and the reference at 1 Gbps.

To demonstrate the operation of the DeMUX, we performed eye diagram measurements. For the measurement, the input was modulated with a non-return-to-zero PRBS signal of $2^{10} - 1$. The inset in Fig. 2 is the eye diagram. The smaller inset is a reference. The eyes are clearly open without any distortion compared with the reference at a speed of 2.5 Gbps.

We also fabricated a device with a 136 GHz spacing and 16 channels, and the results are shown in Ref. [5]

## 4. Crosstalk prevention

In the DeMUX, crosstalk occurs mainly due to the lower resonant peaks in channels at shorter wavelengths as shown in Fig. 2. Figure 3(a) and 3(b) show transmission spectra calculated with 2D-FDTD. The insets show magnified illustrations of one of the channels in the DeMUX. When we applied our fabricated parameters, we obtained the calculated transmittance spectra shown in Fig. 3(a), which agree well with the experimental results. When we shift the output waveguide three columns to the right, we obtain the output spectra shown in Fig. 3(b). While the peak transmittance decreases in Fig. 3(a) as the channel number increases, the peak transmittance becomes higher and remains flat in Fig. 3(b).

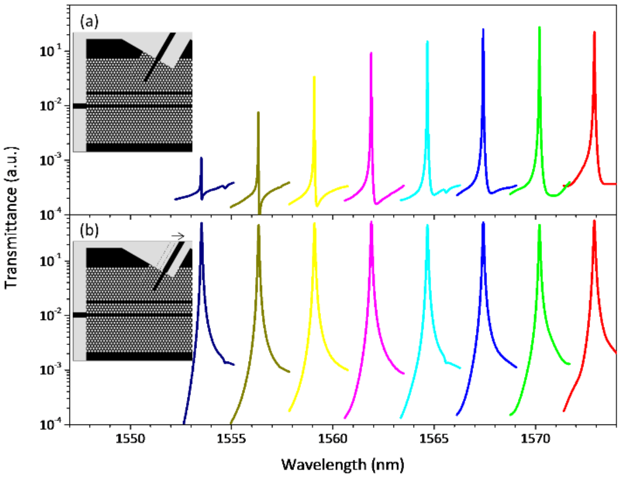


Fig. 3. Transmission spectra calculated with 2D-FDTD simulation. Output waveguides are placed in the same position as in the fabricated structure (a) and are shifted three rows to the right (b). In the 2D-FDTD simulation, we set the effective refractive index of silicon, $n_{eff}$, at 2.81.

## 5. Conclusions

Eight- and 16-channel DeMUXs are demonstrated with spacings of 267 and 136 GHz. The DeMUXs were fabricated photolithographically and clad with silica, which means that they are genuinely compatible with other silicon photonic devices. The PhC DeMUXs are precisely tunable and operate at a speed of 2.5 Gbps. Moreover, they have a footprint of 110 μm$^2$ per channel, which is very much smaller than conventional AWG-based DeMUXs.

## References

1. S. Cheung, T. Su, K. Okamoto, and S. J. B. Yoo, "Ultra-compact silicon photonic 512 × 512 25 GHz arrayed waveguide grating router," IEEE J. Sel. Top. Quantum Electron. **20**, 8202207 (2014).
2. Y. Takahashi, T. Asano, D. Yamashita, and S. Noda, "Ultra-compact 32-channel drop filter with 100 GHz spacing," Opt. Express **22**, 4692–4698 (2014).
3. A. Shinya, S. Mitsugi, E. Kuramochi, and M. Notomi, "Ultrasmall multi-port channel drop filter in two-dimensional photonic crystal on silicon-on-insulator substrate," Opt. Express **14**, 12394–12400 (2006).
4. Y. Ooka, T. Tetsumoto, A. Fushimi, W. Yoshiki, and T. Tanabe, "CMOS compatible high-Q photonic crystal nanocavity fabricated with photolithography on silicon photonic platform," Sci. Rep. **5**, 11312 (2015).
5. Y. Ooka, T. Tetsumoto, N. A. B. Daud, and T. Tanabe, "Ultrasmall in-plane photonic crystal demultiplexers fabricated with photolithography," Opt. Express **25**, 1521–1528 (2017).

# CMOS compatible photo-receiver based on *p-i-n* integrated photonic crystal nanocavity fabricated with photolithography

Nurul Ashikin Binti Daud (D3), Yuta Ooka (M2), Tomohiro Tetsumoto (D3)

We fabricate and demonstrate a high-$Q$ PhC nanocavity with a p-i-n junction as a photoreceiver. We achieve a measured dark current of only 12 pA at a bias voltage of -3 V. With the aid of two-photon absorption, we obtained an internal responsivity for the photodetector of 0.0133 A/W. The PhC nanocavity device was fabricated with a photolithographic fabrication process, which is CMOS compatible and constitutes an advance in silicon PhC nanocavity technologies.

**Key words:** Photonic crystal; Photoreceiver; Opto-electronics; Integrated optics

## 1. Introduction

Silicon photonics has recently become the leading candidate for realizing optical interconnects thanks to its ease of combination with complementary metal-oxide semiconductor (CMOS) electronic fabrication technology [1], [2]. The low operating power and capacity for the integration of silicon photonics has expanded the field of optical interconnect research. However, Si is not an efficient candidate in terms of telecom-light detection. Many researchers have used various methods in an effort to overcome this problem [3-6]. However, reducing the value of the dark current still remains a challenge. Two-photon absorption has been employed due to its low noise and ease of fabrication using a *p-i-n* integrated Si waveguide [7]. Nevertheless, it requires a high optical input. A photonic crystal (PhC) nanocavity with a high $Q$ factor allows us to achieve a high photon density even at very low input power thus making it a good candidate. Furthermore, a numerical study has proved that a *p-i-n* Si PhC nanocavity can achieve a high-speed highly efficient photoreceiver [8].

This report describes a PhC nanocavity as a photoreceiver that constitutes an improvement on the work reported by Tabata in 2015. We show that a PhC nanocavity photoreceiver fabricated by photolithography is comparable to those previously reported that were fabricated with an electro-beam (EB) lithography process [9].

## 2. Device structure

Figure 1 (a) shows a schematic illustration of our device. Input and output waveguides are coupled through barrier line defects with a width of W 1.05. A width modulated line defect for the device is formed along a W 0.98 waveguide and is sandwiched by the $p$ and $n$ regions. The length of the barrier W 0.98 is shown as $d$. The cavity was created by slightly shifting the center part of the waveguide air holes (shift = 3, 6 and 9 nm) towards the outside. There are no additional dopants in the cavity region, so it functions as the $i$ region in the device. The lattice constant $a$, hole radius $r$ and slab thickness $t$ of the PhC are 420, 256 and 210 nm, respectively. The size of the contact aluminum pad is about 45 μm×25 μm. The distance between $p^+$ and $n+$ ion-implanted regions is shown as $w_c$ = 8.9 μm. The width and distance between the $p$ and $n$ regions are shown as $w_w$ and $w_i$. The parameters are $w_i$ = 2.9 μm and $w_w$ = 1.68 μm. The doping densities for the $p$ and $n$ regions are $2.4\times10^{17}$ cm$^{-3}$ and $1.4\times10^{17}$ cm$^{-3}$, respectively.

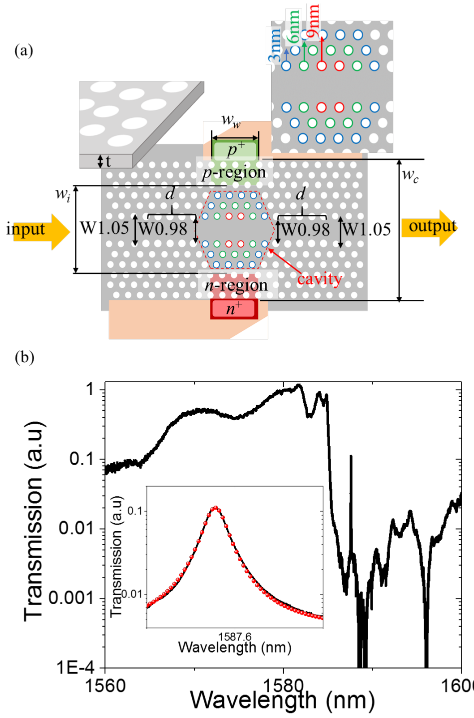


Fig. 1: (a) Schematic illustration of a two-dimensional width modulated line defect PhC nanocavity. (b) Transmittance spectrum of the device. The inset shows the Lorentzian fitting of the peak. The solid black line and dotted red line represent the transmission spectrum and Lorentzian fitting, respectively.

Figure 1 (b) shows the measured spectrum of the device. It exhibits a very high loaded $Q$ of $1.9\times10^5$ at a peak wavelength of around 1587.59 nm. It should be noted that we obtained the high $Q$ value with a silicon PhC nanocavity device realized with a photolithographic fabrication process and clad with $SiO_2$, which makes the structure stable, robust and compatible with CMOS.

## 3. Photoreceiver characteristics

Next, we measured the transmission spectrum and photocurrent at the resonance wavelength. The input optical power was 10 μW. The result at different input wavelengths is shown in Fig. 2. When the light was on resonance, two-photon absorption occurred and photocarriers were generated. Although such a nonlinear detector usually has low efficiency due to the small $\chi^{(3)}$ coefficient of the material, this device exhibited a very high detection efficiency due to the strong light confinement (high $Q$).

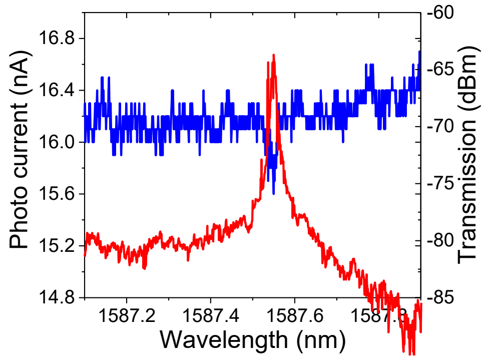


Fig. 2: Transmission spectrum and photo current at resonance wavelength when input power is 10 μW.

Figure 3 shows the responsivity of the device. We increased the input power from -50 dBm to 10 dBm and measured the f photocurrent. The measured internal responsivity of the photodetector was 0.0134 A/W. The external quantum efficiency (QE) of the device was 2.17 % when the input power was 0.316 mW.

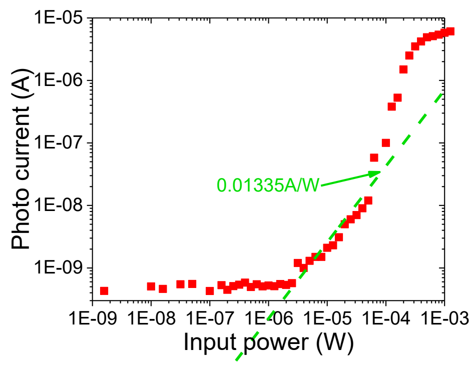


Fig. 3: Photocurrent vs input power when the input laser is at the resonance of the cavity. The dotted green lines show the responsivities at different A/W values.

We further investigated other aspects of the photodetector by measuring the dark current of the device. Figure 4 shows the dark current when the bias voltage is increased from -6 V to 0 V.

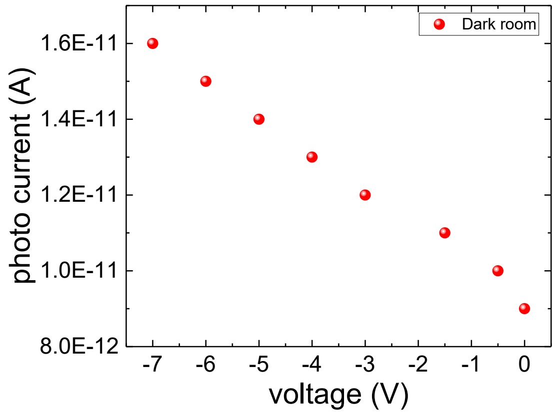


- Fig. 4: Dark current of the device when a reverse bias voltage of -7 V to 0 V is applied to the device.

At a -3 V reverse bias voltage, the measured dark current was 12 pA. This value is smaller than previously reported detectors [3-7]. We achieved a small dark current because of the good crystal quality of the Si and the small dimensions of our *p-i-n* structure.

## 4. Future task

In terms of photodetector application, we need to demonstrate the speed of the receiver. A cavity with a lower $Q$ should be chosen to ensure that the device can be operated at a higher optical input without exhibiting the thermo-optic effect. A low transimpedance gain should be used for this demonstration. The injected signal wavelength will be at the cavity resonance and detuned from the cavity resonance.

## 5. Summary

In summary, we have reported the first demonstration of a PhC nanocavity integrated with a *p-i-n* junction and $SiO_2$ cladding as a photodetector. The device was fabricated by a photolithography fabrication process, which is CMOS compatible and this constitutes an advance in silicon PhC nanocavity technology.

## References

[1] G. Reed, G. Mashanovich, F. Gardes, and D. Thomson, Nature photonics **4**, no. 8 Aug, 2010.

[2] Z.-Y. Li, D.-X. Xu, W. R. McKinnon, S. Janz, J. H. Schmid, P. Cheben, and J.-Z. Yu, Opt. Express **17**, no. 18, pp. 15947–58, 2009.

[3] T. Yin, R. Cohen, M. Mores, G. Sarid, Y. Chetrit, D. Rubin, and M. Paniccia, Opt. Express **15**, 13965 (2007).

[4] Y. Kang, H. Liu, M. Morse, M. Paniccia, M.

Zadka, S. Litski, G. Sarid, A. Pauchard, Y. Kuo, H. Chen, W. Zaoui, J. Bowers, A. Beling, D. McIntosh, X. Zheng, and J. Campbell, Nat. Photonics **3**, 59 (2009).

[5] Y. Liu, C. Chow, W. Cheng, and H. Tsang, IEEE Photon. Technol. Lett. **18**, 1882 (2006).

[6] M. Geis, S. Spector, M. Grein, R. Schulein, J. Yoon, D. Lennon, and T. Lyszczarz, Opt. Express **17**, 5193 (2009).

[7] T. Liang, H. Tsang, E. Day, J. Brake, A. Knights, and M. Asghari, Appl. Phys. Lett. **81**, 1323 (2002).

[8] J. B. Abad, E. Ippen, and M. Soljačić, Appl. Phys. Lett. **94**, 241103 (2009).

[9] T. Tanabe, H. Sumikura, H. Taniyama, A. Shinya, and M. Notomi, Appl. Phys. Lett. **96**, 101103 (2010).

# Statistical Data

# Publications (Apr. 2016 – Mar. 2017)

## Journal papers

[1] Y. Ooka, N. A. B. Daud, T. Tetsumoto, and T. Tanabe, "Compact resonant electro-optic modulator using randomness of a photonic crystal waveguide," Opt. Express, Vol. 24, No. 10, pp. 11199-11207 (2016).

[2] H. Itobe, Y. Nakagawa, Y. Mizumoto, H. Kangawa, Y. Kakinuma, and T. Tanabe, "Bi-material crystalline whispering gallery mode microcavity structure for thermo-opto-mechanical stabilization," AIP Advances, Vol. 6, No. 5, 055116 (2016).

[3] K. Masuda, S. Moriyama, Y. Morita, K. Komatsu, T. Takagi, T. Hashimoto, N. Miki, T. Tanabe, and H. Maki, "Thermal and quantum phase slips in niobium-nitride nanowires based on suspended carbon nanotubes," Appl. Phys. Lett. Vol. 108, 222601 (2016).

[4] T. Kato, A. C.-Jinnai, T. Nagano, T. Kobatake, R. Suzuki, W. Yoshiki, and T. Tanabe, "Hysteresis behavior of Kerr frequency comb generation in a high-quality-factor whispering gallery mode microcavity," Jpn. J. Appl. Phys. Vol. 55, No. 7, 072201 (2016). (SPOTLIGHTS)

[5] Y. Mizumoto, H. Kangawa, Y. Nakagawa, H. Itobe, T. Tanabe, and Y. Kakinuma, "Influence of nose radius on surface integrity in ultra-precision cylindrical turning of single-crystal calcium fluoride," Procedia CIRP, Vol. 45, 139-142 (2016).

[6] Y. Nakagawa, Y. Mizumoto, T. Kato, T. Kobatake, H. Itobe, Y. Kakinuma, and T. Tanabe, "Dispersion tailoring of a crystalline whispering galley mode microcavity for a wide-spanning optical Kerr frequency comb," J. Opt. Soc. Amer. B, Vol. 33, No. 9, pp. 1913-2920 (2016).

[7] A. Godbole, P. P. Dali. V. Janyani, T. Tanabe, and G. Singh, "All optical scalable logic gates using Si3N4 microring resonators," IEEE J. Sel. Top. Quantum Electron. Vol. 22, No. 6, 5900308 (2016).

[8] S. Vyas, T. Tanabe, G. Singh and M. Tiwari, "Ultraflat broadband supercontinuum in highly nonlinear Ge11.5As24Se64.5 photonic crystal fibres," Ukr. J. Phys. Opt. Vol. 17, No. 3, pp. 132–139 (2016).

[9] A. C.-Jinnai, T. Kato, S. Fujii, T. Nagano, T. Kobatake, and T. Tanabe, "Broad bandwidth third-harmonic generation via four-wave mixing and stimulated Raman scattering in a microcavity," Opt. Express, Vol. 24, No. 23, pp. 26322-26331 (2016).

[10] W. Yoshiki, Y. Honda, M. Kobayashi, T. Tetsumoto, and T. Tanabe, "Kerr-induced controllable adiabatic frequency conversion in an ultra-high Q silica toroid microcavity," Opt. Lett., Vol. 41, No. 23, pp. 5482-5485 (2016).

[11] S. Vyas, T. Tanabe, M. Tiwari, and G. Singh, "Chalcogenide photonic crystal fiber for ultraflat mid-infrared supercontinuum generation," Chin. Opt. Lett., Vol. 14, No. 12, pp. 123201 (5 pages) 2016.

[12] T. Kato, A. Hori, R. Suzuki, S. Fujii, T. Kobatake, and T. Tanabe, "Transverse mode interaction via stimulated Raman scattering comb in a silica microcavity," Opt. Express, Vol. 25, No. 2, pp.

857-866 (2017).
[13] Y. Ooka, T. Tetumoto, N. A. B. Daud, and T. Tanabe, "Ultrasmall in-plane photonic crystal demultiplexers fabricated with photolithography," Opt. Express, Vol. 25, No. 2, pp. 1521-1528 (2017).

## International conferences

[1] N. A. B. Daud, Y. Ooka, and T. Tanabe, "p-i-n integrated photonic crystal nanocavity optical functional device," The 5th Advances Lasers and Photon Sources Conference (ALPS'16), ALPSp14-03, Yokohama, May 17-20 (2016).
[2] R. Suzuki, T. Kato, A. Chen-Jinnai, T. Kobatake, S. Fujii, and T. Tanabe, "Effects with Kerr comb in silica toroid microcavity: Raman scattering and third harmonic generation," The 5th Advances Lasers and Photon Sources Conference (ALPS'16), ALPS1-3, Yokohama, May 17-20 (2016).
[3] S. Fujii, Y. Okabe, W. Yoshiki, T. Kato, A. C. Jinnai, T. Kobatake, and T. Tanabe, "The effect on Kerr comb generation in mode coupled WGM microcavity," CLEO:2016, STu3Q.1, San Jose, June 5-10 (2016).
[4] R. Suzuki, T. Kato, A. C. Jinnai, T. Nagano, T. Kobatake, and T. Tanabe, "Kerr comb generation with suppressed cavity-optomechanical oscillation in toroid microcavity," CLEO:2016, STu3Q.7, San Jose, June 5-10 (2016).
[5] T. Kato, A. C. Jinnai, S. Fujii, and T. Tanabe, "Broadband visible comb generation via third harmonic generation assisted by stimulated Raman scattering," CLEO:2016, STu4Q.2, San Jose, June 5-10 (2016).
[6] T. Kato, T. Kobatake, R. Suzuki, and T.Tanabe, "Analysis of effect of interaction between transverse modes on Kerr frequency comb generation," CLEO:2016, JTu5A.48, San Jose, June 5-10 (2016).
[7] H. Itobe, T. Kobatake, Y. Nakagawa, T. Kato, Y. Mizumoto, H. Kangawa, Y. Kakinuma, and T. Tanabe, "Soliton pulse formation in a calcium fluoride whispering gallery microcavity without frequency sweeping," CLEO:2016, SW1E.2, San Jose, June 5-10 (2016).
[8] T. Tetsumoto, Y. Ooka, and T. Tanabe, "Observation of isolated mode and formation of coupled cavity in fiber coupled PhC cavity platform," The 12th International Symposium on Photonic and Electromagnetic Crystal Structures (PECS-XII), A28, University of York, July 17-21 (2016).
[9] T. Tanabe, T. Tetsumoto, H. Itobe, R. Suzuki, and T. Kato, "Optical nonlinear control at a very low power in ultrahigh‐Q microcavity systems," 2016 International Conference on Optical MEMS and Nanophotonics (IEEE OMN 2016), We2.3, Singapore, July 31-August 4 (2016). (invited)
[10] T. Kato, T. Kobatake, A. J.-Chen, A. Hori, and T. Tanabe, "The Effect of Raman Scattering in Kerr Comb Generation in a Silica Toroidal Microcavity," Progress in Electromagnetics Research Symposium (PIERS2016), 2P_13, Shanghai, August 8-11 (2016).
[11] T. Tanabe, T. Kato, R. Suzuki, and S. Fujii, "Kerr comb generation in a whispering gallery mode microcavity: The effect of mode coupling," Progress in Electromagnetics Research Symposium

(PIERS2016), 2P_13-1, Shanghai, August 8-11 (2016). (invited)

[12] T. Tanabe, T. Tetsumoto, Y. Ooka, and N. A. B. Daud, "Recent progress on high-Q photonic crystal nanocavities: Photolithographic fabrication and reconfigurable 2ystem," Progress in Electromagnetics Research Symposium (PIERS2016), SC3, Shanghai, August 8-11 (2016). (invited)

[13] S. Fujii, T. Kato, A. Hori, Y. Okabe, A. Kubota, T. Tanabe, "Blue light emission via harmonic generation by stimulated Raman scattering in a silica toroid microcavity," Frontiers in Optics/Laser Science Conference (FiO/LS), FTh5G.5, Rochester, October 17-21 (2016).

[14] Y. Ooka, N. A. Daud, T. Tetsumoto, T. Tanabe, "Ultrasmall in-plane photonic crystal demultiplexer fabricated with photolithography," Frontiers in Optics/Laser Science Conference (FiO/LS), FTu2D.3, Rochester, October 17-21 (2016).

[15] Y. Okabe, T. Kato, S. Fujii, R. Suzuki, T. Tanabe, "Numerical modeling of the generation of a Kerr comb in a coupled cavity system using coupled mode equations," Frontiers in Optics/Laser Science Conference (FiO/LS), JW2A.150, Rochester, October 17-21 (2016).

[16] T. Tanabe, T. Kato, S. Fujii, R. Suzuki, and A. Hori, "Effect of Raman scattering and mode coupling in Kerr comb generation in a silica whispering gallery mode microcavity," SPIE Photonics West, San Francisco, January 28-February 2 (2017). [Proc. SPIE, Vol. 10090, 100900F (2017).] (invited)

# Dissertations

### PhD thesis:

Takumi Kato, “Nonlinear optical processes with a silica toroid microcavity for optical frequency comb generation,” Mar. 2017.
Wataru Yoshiki, “Dynamic control of ultra-high Q silica toroid optical microcavities,” Feb. 2017.

### Master thesis:

Hiroki Itobe “Optimization of dispersion and thermal characteristics in a calcium fluoride microcavity”
Yuta Ooka “Photonic crystal devices fabricated with photolithography”
Yusuke Okabe “Theoretical study on optical Kerr comb generation in normal dispersion regime using coupled microresontaots”
Misako Kobayashi “Study on Ammonia Gas Sensing using a Silica Toroid Microcavity”
Takuma Nagano “Research on dispersion compensation and phase control of optical Kerr comb”

### Bachelor thesis:

Taku Okamura “Study on the detection of bovine serum albumin using silica toroid microcavity”
Naotaka Okamura “Development of Finite-difference time-domain method of non-diagonal dielectric tensor”
Akihiro Kubota “Fabrication of silica-rod microresonator and observation of third-order nonlinearities”
Mika Fuchida “Precise measurement of dispersion of ultrahigh-Q optical cavity”
Akihiko Honda “Brillouin lasing in silica-toroid coupled resonators”

# Seminars

Date: June 21, 2016
Speaker: Dr. Martin Fermann (IMRA America, USA)
Title: Fiber frequency combs for the real world

Date: December 14, 2016
Speaker: Dr. Ingo Breunig (IMTEX, Freiburg University, Germany)
Title: Continuous-wave optical parametric oscillators: From bow-ties to whispering galleries

Date: January 11, 2017
Speaker: Prof. Marko Loncar (Harvard University, USA)
Title: Quantum/nonlinear photonics with diamonds

Date: February 10, 2017
Speaker: Tsutaru Kumagai (Tokyo Institute of Technology)
Title: Glass silica sphere microresonator for realizing degenerate WGM resonances

Date: March 2, 2017
Speaker: Dr. Philipp Schneeweiss (Technische Universität Wien, Austria)
Title: Integrated quantum optics with cold atoms